ACS MATERIALS LETTERS

www.acsmaterialsletters.org

REVIEW

Excitonic Lasers in Atomically Thin 2D Semiconductors

Wen Wen, Lishu Wu, and Ting Yu*

Cite This: ACS Materials Lett. 2020, 2, 1328–1342

Read Online

ACCESS | Metrics & More | Article Recommendations

ABSTRACT: Two-dimensional (2D) atomically thin transition-metal dichalcogenides (TMD) and their van der Waals (vdW) heterostructures offer a platform with tightly bound intralayer/interlayer excitons for the on-chip fabrication of ultracompact nanolasers. Excitons in 2D TMD materials present a considerable binding energy of up to hundreds of meV, which permits a high Mott transition density of 10^{14} cm^{-2} and stable excitonic lasing under room-temperature operation and high pump fluences. Here, we review the recent progress on the lasing emission from intralayer excitons in TMD monolayers and interlayer excitons in vdW heterostructures incorporated with various high-quality optical cavities, including photonic-crystal, whispering-gallery-mode, distributed-feedback, distributed-Bragg-reflector cavities. Lasing emissions in TMD monolayers and heterostructures have been demonstrated by narrow emission peaks, a clear threshold for nonlinear amplification, time- and spatial coherence under either continuous-wave or pulsed light pumping. Finally, prospective and frontier research topics, including large-scale on-chip integration of TMD nanolasers, electrically pumped lasers, spin-polarized nanolasers, and exciton−polariton Bose−Einstein condensation (BEC) are highlighted.

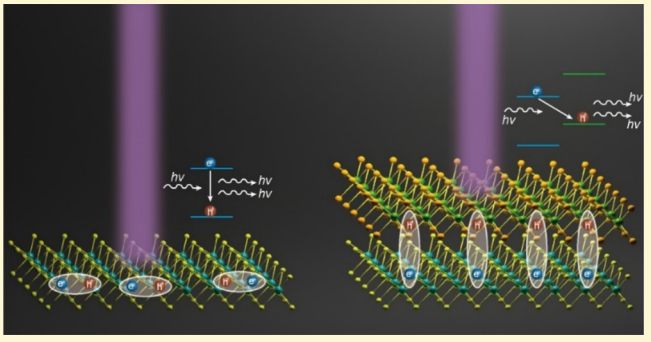

Two-dimensional (2D) atomically thin transition-metal dichalcogenides (TMDs), MX_2 (M is Mo or W; X is S, Se, or Te), are intriguing semiconductors with emission bandgaps ranging from the visible to the near infrared region,[1−3] contrary to graphene with zero bandgap. In their monolayer limit, they have been reported to own direct bandgaps,[4−6] strong excitonic effect with tightly bound excitons,[7−9] strong light−matter interaction,[10] spin−valley locking,[11−20] and considerable charge carrier mobility,[21−23] which envisage unique electronic, photonic and optoelectronic applications, such as field-effect transistors,[24−26] light-emitting diodes,[27−30] optical modulators,[31,32] and nanolasers.[33,34] In 2010, the research into optical properties of TMDs began with the discovery of indirect-to-direct bandgap transition from bulk to monolayer crystals, which results in orders of magnitude improvement of photoluminescence (PL) quantum efficiency from bulks to monolayers.[5,6] In 2012, the discovery of spin−valley locking originating from broken inversion symmetry and strong spin−orbit coupling offers new opportunities for the accessibility to explore valleytronic applications that make use of the spin and valley degrees of freedom in TMD monolayers.[13,14]

Beyond TMD monolayers, van der Waals (vdW) heterostructures constructed by stacking of diverse atomically thin materials, including semi-metallic graphene, insulating hexagonal boron nitride (hBN), TMDs, and other layered materials, provide a novel platform to investigate the exciton excited states, carrier dynamics, spin−valley coupling and moiré potentials.[35−46] Meanwhile, vdW heterostructures also offer a new paradigm to design the superior properties of materials and functionalities of devices because the material properties can be tuned by constituent layers, stacking sequence,[30,47,48] crystallographic orientation,[49−51] and external fields.[52−56] In the vdW heterostructures composed of TMDs, interlayer excitons can be created through either ultrafast charge transfer in optical

> The considerably high exciton binding energy in TMD monolayers permits stable excitons under relatively high population and sustains excitonic lasing emissions.

Received: June 22, 2020
Accepted: September 2, 2020
Published: September 2, 2020

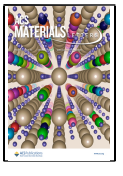

https://dx.doi.org/10.1021/acsmaterialslett.0c00277
ACS Materials Lett. 2020, 2, 1328−1342

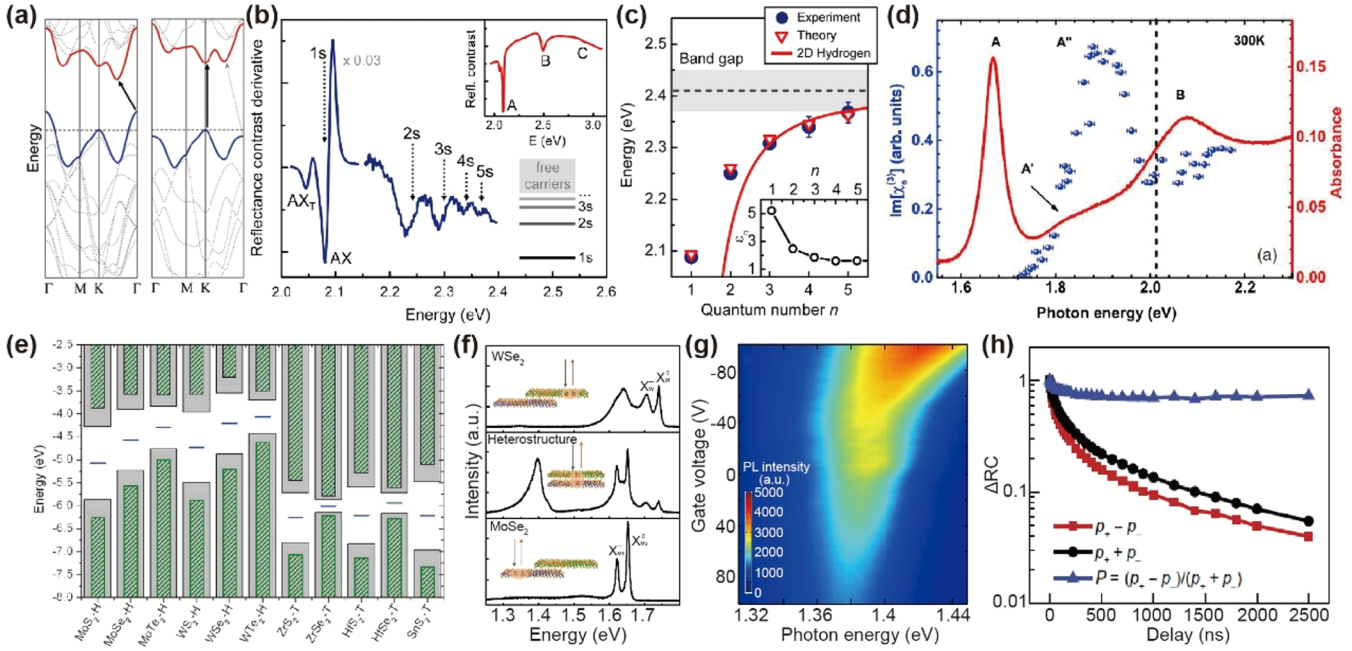

Figure 1. Excitons in TMD monolayers and heterostructures. (a) Calculated electronic band structure of bulk (left) and monolayer (right) MoS_2. Reproduced from ref 5. Copyright 2010 ACS. (b) Derivative reflectance contrast spectrum of the WS_2 monolayer illustrates excitonic Rydberg states. (c) Experimentally measured and theoretically calculated transition energies of exciton states. The solid line shows the fit of n = 3, 4, 5 states to the 2D hydrogen model for Wannier excitons. Inset presents effective dielectric constants. Panels b and c: Reproduced from ref 8. Copyright 2014 APS. (d) Linear absorption (red line) and 2PPL excitation spectra of monolayer WSe_2 collected at room temperature. Reproduced from ref 7. Copyright 2014 APS. (e) Band edges of representative TMDs calculated by PBE-SOC (filled grey) and GW (narrower olive) methods. Reproduced from ref 75. Copyright 2017 IOP. (f) PL emissions of WSe_2, $MoSe_2$, and WSe_2−$MoSe_2$ heterostructure. Emergent PL peak at 1.4 eV indicates the interlayer excitons in WSe_2−$MoSe_2$ heterostructure. (g) PL emission of WSe_2−$MoSe_2$ heterobilayer as a function of applied out-of-plane gate voltage. Panels f and g: Reproduced from ref 57. Copyright 2015 Springer Nature. (h) Dynamics of total hole population ($p_+ + p_-$), valley polarized hole populations ($p_+ + p_-$) and polarization degree (P) show a hole population lifetime exceeding 1 μs and valley polarization lifetime of more than 40 μs. Reproduced from ref 60. Copyright 2017 AAAS.

excitation process or direct electrical injection of electrons/holes into two separated layers.[37,39,42,53,57−59] Compared to their intralayer counterparts, interlayer excitons feature longer lifetime,[57] directional dipole,[52] and longer valley polarization lifetime,[60] which allow for the long-range exciton diffusion, tunable carrier dynamics by electrostatic gating and manipulation of spin-polarized carriers at different valleys.[42,56,61,62]

In addition, on the basis of these atomically thin materials with tightly bound excitons, ultracompact on-chip lasers have been developed. In 2015, the first demonstration of lasing emissions was reported in WSe_2 incorporated with a photonic crystal cavity.[33] After then, the lasing emissions of TMD monolayers and heterostructures have been also implemented by using photonic-crystal,[33,63,64] distributed-feedback,[65] distributed-Bragg-reflector,[66] and whispering-gallery-mode cavities.[34,67] By the material engineering and optical cavity optimization, continuous-wave lasing emissions with a relatively low threshold at room temperature have been realized on both monolayers and vdW heterostructures. In this Review, we summarize recent progress in atomically thin 2D nanolasers based on TMD monolayers and heterostructures. Firstly, we briefly introduce the properties of intralayer excitons in TMD monolayers and interlayer excitons in vdW heterostructures. Secondly, the atomically thin lasers based on intralayer excitons and various optical cavities are discussed. Thirdly, lasing emission and Bose−Einstein condensation (BEC) from interlayer excitons in vdW heterostructures are discussed. We describe the material fabrication, optical cavity design, and lasing performance of lasers based on TMD monolayers and heterostructures. The lasing emissions in TMD materials have been characterized by a narrowed peak, a threshold in the output intensity, and emergent spatial coherence. We conclude the Review by highlighting the future research directions, including exciton−polariton lasers, spin lasers, electrically pumped lasers and scalable fabrication of lasers based on TMD materials.

EXCITONS IN TMD MONOLAYERS AND HETEROSTRUCTURES

The excitons in TMD monolayers and heterostructures have attracted intense attention owing to the following features. First, TMDs undergo a transition from an indirect to a direct bandgap, when the thickness of TMDs is thinned down to monolayers (Figure 1a),[5] which is reflected by a great enhancement of PL quantum efficiency with a factor of exceeding 10^4 in monolayers.

Second, the stable excitons with a large binding energy of hundreds of meV have been demonstrated, which is attributed to the quantum confinement effect and significantly reduced dielectric screening in TMD monolayers (Figure 1b−d). Heinz and his colleagues discovered the excitonic Rydberg series (n = 1−5) through reflectance spectra in WS_2 monolayers (Figure 1b).[8] The n = 3−5 peaks can be fitted by a 2D hydrogen model. Exciton transition energies can be calculated by bandgap (E_g) and exciton binding energy of nth excitonic state ($E_b^{(n)}$) as $E_g - E^{(n)}$ and $E_b^{(n)}$ can be expressed as

$$E_b^{(n)} = \frac{\mu e^4}{2\hbar\varepsilon(n - 1/2)^2} \quad (1)$$

https://dx.doi.org/10.1021/acsmaterialslett.0c00277
ACS Materials Lett. 2020, 2, 1328−1342

where μ is the reduced mass of exciton and ε is the permittivity. The model is well fitted with n = 3−5 excitons and indicates a bandgap of E_g = 2.41 ± 0.04 eV, and the exciton binding energy of the 1s exciton state is 0.32 ± 0.04 eV by considering its exciton transition energy of 2.09 eV (Figure 1c). The non-hydrogenic physics of n = 1, 2 excitons are caused by the higher effective dielectric constants of excitons with low quantum numbers (Figure 1c inset). Shan and her colleagues demonstrated the measurement of band-to-band transition in WSe_2 monolayers by combining linear absorption and two-photon PL (2PPL) excitation spectra (Figure 1d).[7] While linear absorption could not identify a clear band-to-band transition, the 2PPL excitation spectrum can be well fitted by an exciton peak related to the superposition of p states and a band-to-band transition with E_g = 2.02 eV. The binding energy of 1s excitons was calculated as 0.37 eV based on the 1s exciton transition energy and band-to-band transition energy. The considerable high exciton binding energy in TMD monolayers permits stable excitons under relatively high population and sustains excitonic lasing emissions.

Third, broken inversion symmetry and strong spin−orbit coupling cause spin−valley locking, which gives rise to intriguing properties, such as valley Hall effect,[11,69,70] valley polarized excitons,[42] valley Zeeman,[71−73] and AC stark effects.[15] Valley polarized lasing emission has yet been realized in TMDs possibly because of the depolarization caused by the electron−hole exchange interaction, which is enhanced under high exciton population. Therefore, in this Review, we will not further discuss the spin−valley polarization and some comprehensive reviews on this topic are recommended.[4,18,74]

Fourth, atomically sharp heterostructures can be constructed by stacking different kinds of TMD layers. The library of 2D TMDs allows for constructing type-II heterostructures, which support ultrafast charge transfer and formation of interlayer excitons.[75] Density functional theory (DFT) calculations have been performed to predict the band edges of TMD monolayers, which has provided guidelines for the construction of type-II heterostructures (Figure 1e).[68,75] Before the discovery of interlayer excitons, the ultrafast charge transfer has been demonstrated by Wang and his colleagues in type-II MoS_2/WS_2 heterobilayers.[37] PL mapping demonstrated a strongly quenched PL in the heterostructure region, indicating the efficient charge transfer. By using femtosecond pump-probe spectroscopy, ultrafast hole transfer from MoS_2 to WS_2 at a time scale of within 50 fs has been revealed. The ultrafast charge transfer in heterostructures enables the buildup of a high population of interlayer excitons before the recombination of intralayer excitons. Xu and his colleagues firstly reported the formation of interlayer excitons between WSe_2−$MoSe_2$ heterobilayers (Figure 1f).[57] PL spectrum of WSe_2−$MoSe_2$ shows an interlayer exciton peak at lower energy of 1.4 eV, while the emissions of neutral (X^0) and charged (X^-) excitons range from 1.55 to 1.75 eV. Interlayer excitons with electrons in $MoSe_2$ and holes in WSe_2 exhibit directional dipoles from $MoSe_2$ to WSe_2, which supports tuning of excitonic emission by electric field (Figure 1g). Compared to the rapid exciton recombination with the lifetime of 3−100 ps, the interlayer excitons present a much longer lifetime of over 1 μs (Figure 1h).[60] More importantly, exciton−hole exchange interaction for the depolarization process is suppressed owing to the spatial separation of electrons and holes, yielding an ultralong valley polarization lifetime of 40 μs.[60] Interlayer excitons with electrons and holes in two separated layers have been demonstrated with longer carrier lifetime, valley polarization lifetime, tunable polarization by electric field and controllable carrier species and dynamics through electrical injection. Therefore, interlayer excitons are promising candidates to be used in spin lasers and electrically pumped lasers based on TMD heterostructures.

> The ultrafast charge transfer in heterostructures enables the buildup of a high population of interlayer excitons before the recombination of intralayer excitons.

LASING EMISSION IN TMD MONOLAYERS

Lasers comprise gain media for stimulated photon emission and optical cavities for confinement and resonant recirculation of light.[76] As an ultrathin quantum emitter, monolayer TMD is a category of high-performance gain media with unique advantages of small footprints, low power consumption, efficient coupling with microcavities, and feasible on-chip integration.[3] TMD monolayers possess tightly-bound excitons with binding energy of exceeding 0.3 eV.[4] Such a large binding energy sustain stable excitons at the room temperature and high Mott transition density of ~10^{14} cm^{-2}. Therefore, stable excitons can be preserved even at the pump fluence level for achieving population inversion. These excitons also possess high radiative recombination quantum efficiency owing to the intrinsic direct bandgap in TMD monolayers.[5,6] Strong excitonic resonance and small Bohr radius also benefit efficient and fast radiative recombination, which is important for the buildup of population inversion. For TMD monolayer lasers, the design and optimization of optical cavities are crucial for realizing low-threshold lasing emission. Because of their ultrathin size, TMD monolayers are not capable of confining emitted photons, which requires additional optical cavities to sustain high optical gain. In this section, we will review lasers constructed by TMD monolayers as gain media and different optical cavities. Before the discussion of specific reports, we would like to recommend the Commentary Article on the criteria of lasing emission, which include narrow line width, clear threshold, small beam divergence, polarization, and spatial and temporal coherence.[77]

> Because of their ultrathin size, TMD monolayers are not capable of confining emitted photons, which requires additional optical cavities to sustain high optical gain.

PHOTONIC CRYSTAL LASERS

Photonic crystal cavities are usually fabricated by etching periodic structures on membranes with high refractive indexes.[78] These periodic structures show tunable photonic bandgaps, which prevent light propagation at corresponding frequencies. By introducing defects in periodic structures, strong confinement of electromagnetic field can be realized, yielding microcavities with small volumes and large quality factors exceeding 10^5.[79] Therefore, photonic-crystal cavities have shown broad applications in optically/electrically pumped

https://dx.doi.org/10.1021/acsmaterialslett.0c00277
ACS Materials Lett. 2020, 2, 1328−1342

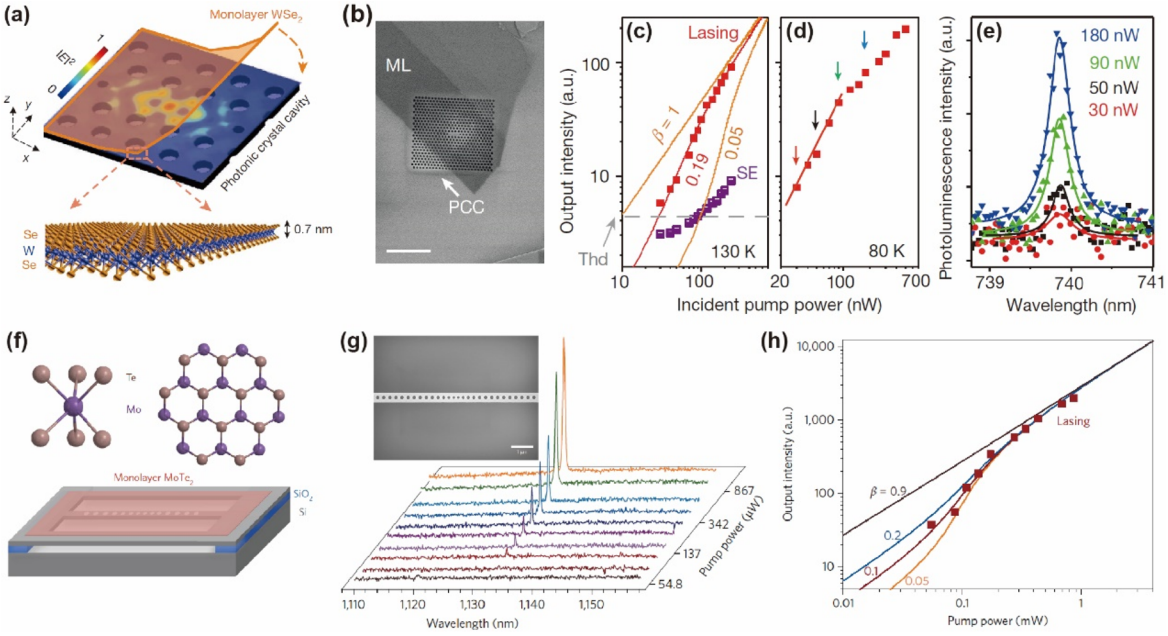

Figure 2. Lasers based on TMD monolayers and photonic-crystal cavities. (a) Schematic illustration of monolayer WSe_2 onto photonic-crystal cavities. (b) SEM image presents a WSe_2 monolayer on photonic crystal. Output intensity of the TMD monolayer laser as a function of incident pump power at (c) 130 and (d) 80 K. (e) Representative photoluminescence spectra at pump powers labeled in panel d. Panels a–e: Reproduced from ref 33. Copyright 2015 Springer Nature. (f) Scheme of $MoTe_2$ monolayer onto a Si photonic crystal suspended in air. (g) Power-dependent photoluminescence spectra of a $MoTe_2$ laser at room temperature. Inset is a SEM image of a suspended photonic crystal. (h) Output intensity of a $MoTe_2$ laser as a function of pump power. The solid lines are fitted results by rate equation with different spontaneous emission factors β. Panels f–h: Reproduced from ref 64. Copyright 2017 Springer Nature.

nanolasers, cavity quantum electrodynamics and single-photon sources. The photonic crystal cavities have enabled the fabrication of high-performance nanolasers with low thresholds, high quality factors and ultrafast modulation.[80−83] For instance, quantum dots, a kind of quantum emitters with ultrasmall mode volume, have been incorporated into photonic crystal cavities to create nanolasers.[84,85] Photonic crystals also provide a platform for the integrated photonics based on 2D materials. Nanolasers, waveguides, interferometers, modulators, and photodetectors can be integrated onto a photonic-crystal chip to build photonic logic devices.[32,86,87]

The first TMD-monolayer laser was reported by Xu and his colleagues in 2015.[33] This nanolaser was constructed by loading a mechanically exfoliated WSe_2 monolayer onto a photonic-crystal cavity (Figure 2a, b). To ensure the high gain and low loss, a L3-type photonic crystal cavity was fabricated on a gallium phosphide (GaP) thin membrane, which is transparent to WSe_2. This photonic crystal cavity presented a quality factor of about 10^4, which created strong local optical density of states. Power-dependent PL measurements unambiguously demonstrated lasing emission of this TMD monolayer laser. At 80 and 130 K, a clear "kink" has been observed in the pump-power-dependent output intensity curves (Figure 2c, d). In contrast, the intensities of spontaneous emission presented no obvious "kink" as a function of pump power. The power-dependent intensity can be fitted by the rate equation as follows

$$R_{ex} = \frac{P}{\Gamma t_c(1 + aP)}\left(\frac{1}{\beta} + aP\right) \quad (2)$$

where R_{ex} is the optical pumping rate, P is the cavity photon number, Γ is the cavity confinement factor, a is a coefficient, β factor is defined as the fraction of spontaneous emission into the cavity mode. A β factor of 0.19 is best fitted for the power-dependent output intensity curve. The line width of PL peak is also dependent on the pump power (Figure 2e). With the increase of pump power, line width of PL peak experienced a narrowing from 0.75 to 0.55 nm below the threshold. Across the threshold regime, a slight broadening of line width to 0.65 nm occurred and then the line width continuously decreased to 0.55 nm above the threshold. The broadening of line width in threshold regime can be attributed to the coupling between intensity and phase noise during the transition from spontaneous emission to stimulated emission, which has been observed in other photonic-crystal lasers based on quantum dots and quantum wells. This nanolaser also presented localized lasing emission at the defect sites in the photonic crystal. At the defect site, narrow PL peak related to stimulated emission of WSe_2 in cavity can be observed. In contrast, a broad PL peak related to spontaneous emission from WSe_2 can be observed in the off-cavity region. This work demonstrated, for the first time, that lasing emission can be realized on an ultrathin quantum emitter with stable excitons.

Silicon photonic crystal cavities are not suitable for the fabrication of nanolasers based on MoS_2, WS_2, $MoSe_2$, and WSe_2 because of the strong absorption of photons with energy higher than 1.1 eV for silicon.

The above reported nanolaser based on WSe_2 and GaP photonic crystal cavities can only be operated at cryogenic temperature, as the room-temperature operation of this

https://dx.doi.org/10.1021/acsmaterialslett.0c00277
ACS Materials Lett. 2020, 2, 1328−1342

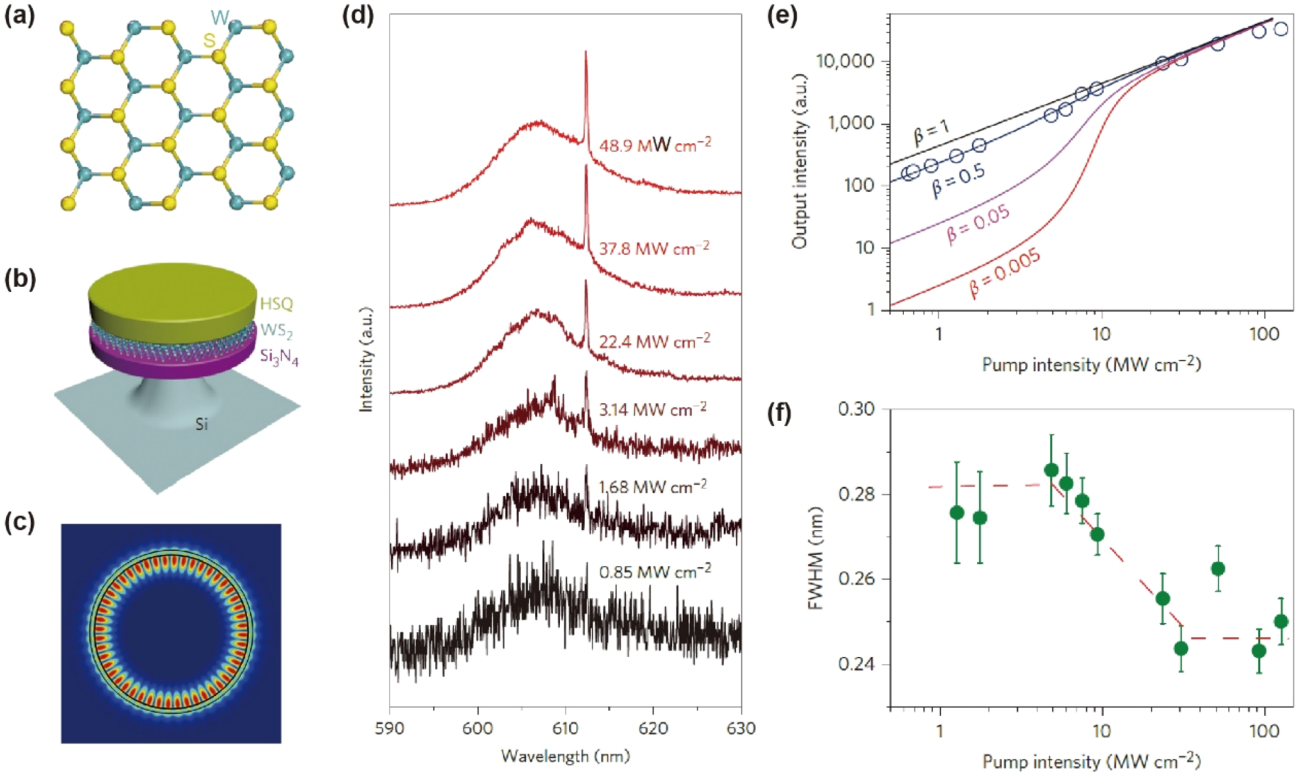

Figure 3. TMD monolayer nanolasers based on whispering gallery mode cavities. (a) Scheme of the crystal structure of WS_2 monolayer. (b) Illustration of microdisk laser based on WS_2 monolayer. (c) Simulated electric field distribution of TE resonance in a microdisk cavity. (d) PL spectra of WS_2 nanolaser under different pump intensities, showing a narrow lasing peak when pump intensity is above the threshold. (e) Output intensity of WS_2 nanolaser as a function of pump intensity. The solid lines indicate the fitting of data by rate equation. (f) FWHM of a monolayer WS_2 laser as a function of pump intensity. Reproduced from ref 34. Copyright 2015 Springer Nature.

nanolaser might be limited by its relatively low quality factor. Silicon exhibits a high refractive index of 3.4 and matured fabrication techniques for the construction of photonic crystal structures. However, silicon photonic crystal cavities are not suitable for the fabrication of nanolasers based on MoS_2, WS_2, $MoSe_2$, and WSe_2, owing to the strong absorption of photons with energy higher than 1.1 eV for silicon. The self-absorption introduces large losses in cavities, which is detrimental to the lasing emission. Ning and his colleagues circumvented this restriction and reported a room-temperature nanolaser based on silicon photonic cavity by employing monolayer $MoTe_2$ as gain media.[64] Monolayer $MoTe_2$ exhibits an excitonic emission peak at ~1.1 eV, which is 50 meV below the bandgap of silicon. By covering monolayer $MoTe_2$ onto silicon photonic crystal (Figure 2f), infrared lasing emissions were realized at room temperature.

The photonic crystal cavity was fabricated by electron-beam lithography and etching on a silicon-on-insulator chip, yielding a suspended nanobeam structure (Figure 2g, inset). This nanobeam cavity contained 10 periods of holes at each side as "mirror" sections, while 8 holes with gradually decreased size served as a cavity. This photonic crystal cavity presents three resonant cavity modes at wavelength of 1054, 1132, and 1167 nm with quality factor of 5.2×10^6, 6.5×10^5, and 1.4×10^3, respectively. An exfoliated $MoTe_2$ monolayer was directly transferred onto the nanobeam cavity to construct a nanolaser. The nanolaser was pumped by a 633 nm continuous-wave laser at room temperature. With the increase of pumped power, a narrow PL peak at 1132 nm can be observed, indicating the lasing emission (Figure 2g). The full width at half maximum (FWHM) is 0.202 nm, corresponding to a quality factor of 5603. This quality factor is higher than that of 2465 observed in the GaP cavity at cryogenic temperature. The greatly enhanced quality factor enables lasing emission at room temperature. The output intensities present an obvious threshold of 0.097 mW with the increase of pumped power. The output-intensity curve can be fitted by rate equation with a β factor of 0.1. In summary, this work demonstrated a low-threshold infrared laser based on a $MoTe_2$ monolayer and suspended photonic crystal cavity, which highlights the importance of high-quality factor of cavity to the high-performance nanolasers.

WHISPERING GALLERY MODE LASERS

Whispering gallery mode (WGM) microcavities,[76] such as microdisks, microspheres, and optical fibers, have been demonstrated with ultrahigh quality factor for the application of small lasers,[88] chemical/biological sensors,[89,90] and frequency combs.[91,92] Ultrahigh quality factor of exceeding 10^8 have been demonstrated in microdisks and optical fibers,[90,93,94] permitting the realization of low-threshold nanolasers based on TMD monolayers.

Zhang and his colleagues reported a nanolaser by combining a WS_2 monolayer with a WGM cavity. This nanolaser was fabricated by embedding a WS_2 monolayer between dielectric layers of Si_3N_4 and HSQ to form a WGM cavity (Figure 3a, b).[34] By carefully designing microcavity, a microdisk with a diameter of 3.3 μm was employed, presenting a resonant transverse electric (TE)-polarized WGM at a wavelength of 612 nm (Figure 3c). This resonant mode overlapped with the exciton emission peak and showed a high-quality factor of 2604.

https://dx.doi.org/10.1021/acsmaterialslett.0c00277
ACS Materials Lett. 2020, 2, 1328−1342

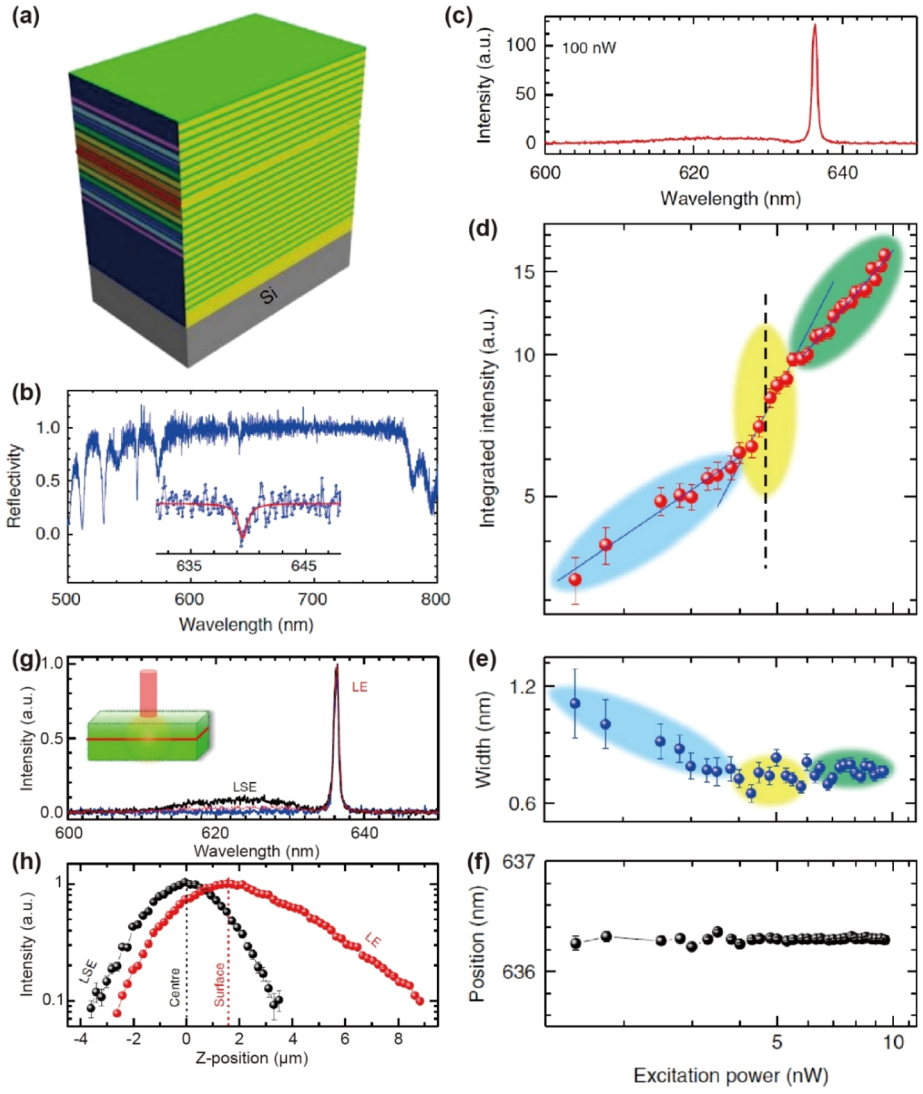

Figure 4. Vertical-cavity surface-emitting lasers based on WS_2 monolayers. (a) Scheme of WS_2 monolayers sandwiched between top and bottom distributed Bragg reflectors (DBRs). (b) Reflection spectra of WS_2 monolayer embedded in DBRs. (c) PL spectrum of WS_2 in a cavity at the excitation power of 100 nW. (d–f) Integrated intensity, width and position of a WS_2 laser as functions of excitation power. (g) Confocal PL scanning at the position of cavity center (black), surface (red), and 5.1 μm (blue), respectively. (h) PL intensities of lasing emission (LE) and leaked spontaneous emission (LSE) at different Z positions. Reproduced from ref 66. Copyright 2017 Springer Nature.

The lasing emissions of WS_2 WGM nanolasers were optically pumped by a 473 nm pulsed laser (190 fs pulse duration, 80 MHz repetition rate) at 10 K. The PL emissions of monolayer WS_2 in cavity shows a clear power dependence: at low pump power intensity below 3.14 MW cm^{-2}, a broad peak corresponding to spontaneous emission of WS_2 was observed; as the power exceeds 22.4 MW cm^{-2}, a narrow peak at 612.2 nm appeared, indicating the lasing emission of WS_2 (Figure 3d). The power-dependent emission intensities of a WS_2 nanolaser has been fitted by rate equation, displaying a threshold of ~5–8 MW cm^{-2} and a β factor of 0.5 (Figure 3e). The FWHM as a function of pump intensity also shows a clear narrowing of peak above threshold, demonstrating the transition from spontaneous emission to stimulated lasing emission (Figure 3f). This work represents the first demonstration of a WGM laser based on TMD monolayers. The ultrahigh quality factors of WGM cavities permit the realization of low-threshold lasing emission. Compared to photonic-crystal nanolasers, which are restricted by the self-absorption in III–V or Si semiconductor nanocavities, the introduction of dielectric WMG cavities also circumvent the restriction of material selection.

Besides the microdisks, other categories of WGM cavities can also be employed to construct high-performance nanolasers based on TMDs. Salehzadeh et al. reported a room-temperature laser with multiple lasing modes based on four-layer MoS_2 and a free-standing microdisk and microsphere cavity.[95] The four-layer MoS_2 was employed and treated with O_2 plasma to obtain a direct bandgap. Compared to monolayers, four-layer MoS_2 were selected by considering the suppressed Auger recombination with the increase of thickness. By sandwiching MoS_2 layers between a microdisk and a microsphere, a confined strong optical field can be achieved at the microdisk/microsphere interface. Through 3D finite-difference time-domain (FTDT) simulation, remarkably enhanced electric field at the interface between the SiO_2 microdisk and microsphere were demonstrated, which benefits optical confinement and realization of low-threshold lasing emission. Multi-mode lasing emissions were observed as the pump power exceeds a threshold of 5 μW.

https://dx.doi.org/10.1021/acsmaterialslett.0c00277
ACS Materials Lett. 2020, 2, 1328–1342

This work demonstrated that lower-threshold and room-temperature lasing emission can be realized by optimizing the microcavity to create a confined strong optical field.

Passivation of TMD monolayers is another significant approach for lowering the threshold and realization of room-temperature operation of lasers.[96−99] Recently, Liao et al. demonstrated a WGM mode laser with a threshold of 5 W cm^{-2} based on chemical vapor deposition (CVD) grown MoS_2.[67] Micro/nanofibers were employed as WGM cavity and MoS_2 were directly grown onto these cavities by a CVD process. The taper-drawing processing was carried out to fabricate micro/nanofiber cavities of 1 μm in diameter from standard fibers of 125 μm in diameter. In this process, the breaking of siloxane bonds occurs to generate oxygen dangling bonds. The authors demonstrated that these dangling bonds can effectively passivate the defects in MoS_2 monolayers under a wide power dynamic range. At low pump power of less than 1 W cm^{-2}, the quantum yield of 30% can be achieved. Even under a high pump power of 10^4 W cm^{-2}, a relatively high quantum efficiency exceeding 1% can be reached. In contrast, the MoS_2 on planar substrate exhibited quantum yield of less than 0.05%. Well passivated defects in MoS_2 benefits the buildup of population inversion at lower power, therefore effectively lowering the lasing threshold of MoS_2. By pumping the MoS_2 WGM lasers with a 532 nm continuous-wave laser, lasing emission can be observed, which presented a low threshold of 5 W cm^{-2} at room temperature. Above the threshold, this WGM laser exhibited a FWHM of ∼1.97 nm, corresponding to a quality factor of 350. This result indicates that low-threshold lasing emissions are feasible based on well passivated monolayers. For the practical application of TMD-based nanolasers, this work is illuminating because the CVD grown samples is important to the scalable fabrication and on-chip integration of nanolasers.

VERTICAL-CAVITY SURFACE-EMITTING LASERS

Vertical-cavity surface-emitting lasers (VCSELs) employs distributed Bragg reflectors (DBRs) to achieve a very high reflectivity and strong confinement of photons in a cavity. DBRs are composed of layers with alternating high and low refractive indices and each layer has an optical thickness of $\lambda/4$, where λ is optical wavelength.[100] These alternating layers can cause destructive interference at each layer interface, thus giving rise to a stop band for light transmission. With these high-performance reflectors, long cavity photon lifetime of several picoseconds and high quality factor exceeding 10^4 have been realized in VCSELs.[101,102] VCSEL geometry has been employed to realize the lasing emission of III−V semiconductors,[103−105] organic materials,[106] colloidal quantum dots,[107] and biological emitters.[108] The optical cavity based on DBRs also provides a platform to study the strong coupling between light and mater.[109−111] Exciton polaritons (EPs) and EP Bose−Einstein condensation have been demonstrated in DBR cavities based on III−V materials,[103] organic semiconductors,[112] and metal-halide perovskites.[113]

VCSEL geometry is also important for the realization of low-threshold lasing emission of TMD monolayers because of its sub-wavelength cavity length and ultrahigh quality factor. Additionally, embedding TMD monolayers into DBRs also isolate active materials from ambient environment, which benefits the operating stability of lasers. In 2017, Yu and his colleagues demonstrated, for the first time, the VCSELs based on WS_2 by continuous-wave excitation at room temperature.[66] The lasers were constructed by embedding WS_2 monolayers into bottom and top DBRs with 12.5 and 8.5 pairs of SiO_2/TiO_2 layers, respectively (Figure 4a). These DBRs creates a stop band for light transmission from 590 to 760 nm, which is illustrated in reflection spectrum (Figure 4b). A dip related to a cavity photon mode can be observed at 639.5 nm with a 1.0 ± 0.2 nm, indicating a quality factor of ca. 640. Therefore, these DBRs are capable to confine photons for creating a high-quality optical cavity. Based on this device configuration, a sharp PL peak at 636.3 nm can be observed by pumping with a 532 nm continuous-wave laser, suggesting the stimulated lasing emission of WS_2 (Figure 1c). The output intensity as a function of pump power illustrates three obvious regions (Figure 1d). In the first region, PL intensity presents a sublinear relationship with pump power, implying spontaneous exciton emission. The sublinear behavior might be caused by side recombination channels, such as exciton−exciton annihilation under high excitation power. As pump fluence exceeds 4 nW, a superlinear dependence can be observed and a nearly linear dependence can be observed when the pump fluence increases up to 6 nW. This nonlinear response of PL emission strongly evidences the buildup of lasing emission in WS_2.

The lasing emission of WS_2 was also demonstrated by the power-dependent line width of PL. With the increase of pump fluence, the line width of PL peak decreases from ∼1.2 nm to ∼0.6 nm, while stabilizes at 0.6 nm above the threshold power of 4 nW. The peak position as a function of power illustrates no obvious blueshift with increased power, indicating that this system is a typical photonic laser, instead of exciton−polariton condensation. The lasing behavior of WS_2 VCSELs was also demonstrated by confocal PL measurements along *Z*-direction. With the focal plane at the cavity centre, both the narrow peak related to lasing emission and a board peak corresponding to leaked spontaneous emission can be observed (Figure 1g). The *Z*-position-dependent PL intensity also indicates that leaked spontaneous emission mainly localized at cavity centre, while the lasing emission is surface emitting. The slower spatial decay of lasing emission indicates its high stability and less diffusion. This work demonstrates low-threshold VCSEL based on TMD monolayers and also creates opportunities to create polariton lasers or electrically pumped lasers based on TMD materials and such a device configuration.

INTERLAYER-EXCITON LASING BASED ON TMD HETEROSTRUCTURES

Ultrafast charge transfer can boost the formation of spatially indirect interlayer excitons with electrons and holes distributed in two different layers in TMD heterostructures. These interlayer excitons possess intriguing optical properties compared to those of direct excitons in monolayers. Firstly, the interlayer excitons exhibit much longer lifetimes than the intralayer excitons. The longer lifetimes permit the relaxation of excitons into ground states before recombination, thus, hopefully, leading to the realization of exciton−polariton BEC and lasing emission. Secondly, electrons and holes distributed in different layers result in permanent electric dipole moment of interlayer excitons, which benefits the stronger repulsive nonlinear interactions and electric-field-tunable carrier dynamics. The spatially separated electrons and holes also allows for the electric injection from different sides of heterojunctions, which boosts the development of light-emitting diodes and possible electrically pumped lasers.

https://dx.doi.org/10.1021/acsmaterialslett.0c00277
ACS Materials Lett. 2020, 2, 1328−1342

PHOTONIC LASING BASED ON INTERLAYER EXCITONS

For the lasing emission, type-II TMD heterostructures provide a three-level system, which benefits the buildup of population inversion and low-threshold lasing emission. More importantly, such a device configuration is hopeful to realize lasing emission via electric injection, which is crucial for practical applications. Meanwhile, the relatively lower quantum efficiency stemming from the momentum mismatch and reduced exciton oscillation strength also might be the restriction for the realization of high-performance lasing emissions based on interlayer excitons.

Interlayer excitons possess intriguing optical properties compared to those of direct excitons in monolayers.

Gao and his colleagues firstly demonstrated the interlayer-exciton lasers based on MoS_2/WSe_2 heterostructures (Figure 5a).[63] The MoS_2 and WSe_2 can forms type-II band alignment. Ultrafast charge transfer has been demonstrated at the time scale within 50 fs, yielding electrons in MoS_2 and holes in WSe_2 to form interlayer excitons. Free-standing photonic crystal cavity comprising 220 nm suspended silicon was selected to confine photons with a high-quality factor and MoS_2/WSe_2 heterostructures were fabricated by dry transfer onto photonic crystals (Figure 5b). The intralayer exciton emissions of MoS_2 and WSe_2 are centred at 668 and 750 nm, respectively. In contrast, the interlayer excitons exhibit a PL peak at 1128.6 nm, which is out of absorption band of silicon. With the pump power exceeding the threshold, a sharp cavity mode of stimulated emissions of heterostructures can be observed at room temperature (Figure 5c). The FWHM of cavity mode slightly above the lasing threshold is 2.15 nm. The output power as a function of pump power provides a strong evidence of lasing emission (Figure 5d). For cavity mode, an obvious "kink" can be observed, which can be attributed to the nonlinear behavior of lasing emission. In contrast, there is no obvious "kink" in broad spontaneous emissions.

Coherence is another important criterion of lasing emission. The coherent length of MoS_2/WSe_2 interlayer-exciton lasers were measured by a Michelson interferometer. The visibility is defined as

$$\nu = \frac{I_{max}(\Delta\tau) - I_{min}(\Delta\tau)}{I_{max}(\Delta\tau) + I_{min}(\Delta\tau)} \quad (3)$$

where $I_{max(min)}$ is the maximum (minimum) intensity of envelop function at delay time of $\Delta\tau$. The measured visibility as a function of path delay is shown in Figure 5e. The visibility contains two components: a fast decay corresponding to spontaneous emission and a broad component related to lasing emissions with longer coherent time. By this method, the coherent time of lasing emissions can be extracted at different pump power (Figure 5f). The coherent time of lasing emission achieves ~1.7 ps when the pump power exceeds ~35 μW, which is consistent with the lasing threshold observed in power-dependent output intensity. With these evidences of spectra, power dependence and coherence, the lasing emission of interlayer excitons in TMD heterostructures was unambiguously demonstrated.

Deng and her colleagues demonstrated an interlayer-exciton laser based on a $WSe_2/MoSe_2$ heterobilayer and a grating cavity.[65] The grating cavity was fabricated onto SiN_x by e-beam lithography and dry etching followed by transferring TMD layers (Figure 5g). To enable the bright interlayer excitons, the axes of WSe_2 and $MoSe_2$ were strictly aligned with rotation angle of below 1°, which prevents the nonradiative loss caused by momentum mismatch. WSe_2 and $MoSe_2$ exhibit a type-II band alignment. Ultrafast electron transfer occurs from the conduction band of WSe_2 to that of $MoSe_2$ on the time scale of 10-100 fs, while the holes are left in WSe_2. A typical PL spectrum of $WSe_2/MoSe_2$ heterobilayer (Figure 5h) illustrates that the intensity of low-energy interlayer exciton peak overwhelms the intralayer excitons of $MoSe_2$ and WSe_2 at higher energy, indicating the efficient charge transfer and buildup of interlayer-exciton population. The lasing emissions of heterobilayers have been demonstrated by calculating the photon occupancy I_p ($k \approx 0$) at different pump power (Figure 5i). When the I_p reaches one, a transition from linear to superlinear increase with the rise of pump power can be observed, indicating the transition from spontaneous to stimulated emissions above the threshold (P_{th} = 0.18 μW). Above the threshold, the line width of lasing emission also experiences a sharp decrease from ~2.4 to ~1.9 meV.

To rigorously identify the lasing behavior, first-order coherence measurements were carried out. The first-order spatial coherence function $g^{(1)}(r_1, r_2)$ is defined as

$$g^{(1)}(\mathbf{r}_1, \mathbf{r}_2) = \frac{G^{(1)}(\mathbf{r}_1, \mathbf{r}_2)}{\sqrt{G^{(1)}(\mathbf{r}_1, \mathbf{r}_2)G^{(1)}(\mathbf{r}_2, \mathbf{r}_1)}} \quad (4)$$

where $G^{(1)}(\mathbf{r}_1, \mathbf{r}_2)$ is the first order correlation function, defined as

$$G^{(1)}(\mathbf{r}_1, \mathbf{r}_2) = \mathrm{Tr}\{\rho E^{(-)}(\mathbf{r}_1)E^{(+)}(\mathbf{r}_2)\} \quad (5)$$

where ρ is the density matrix operator, $E^{(+)}$ and $E^{(-)}$ are field creation, and annihilation operators, respectively. The modulus of coherence degree $|g^{(1)}(\mathbf{r}_1, \mathbf{r}_2)|$ can be directly characterized by the visibility measured in a Michelson interferometer (Figure 5j). A typical interference pattern indicates coherence of emission, thus demonstrating the lasing emission of interlayer excitons in the $WSe_2/MoSe_2$ heterobilayer. The coherence length as a function of pump power (Figure 5l) indicates that the buildup of high-coherence lasing emission as the pump power exceeds the threshold. Overall, lasing emission of interlayer excitons can be realized through optical pumping with rational band alignment and high-quality optical cavity.

BOSE−EINSTEIN CONDENSATION OF INTERLAYER EXCITONS

For dissipative out-of-equilibrium Boson systems, exciton BEC often accompanies with lasing emission, owing to the elementary excitation concentrated into a same ground state. Compared to photonic lasing, which requires population inversion at a relatively high pump density, lasing based on BEC, such as exciton−polariton lasing, often exhibits much lower threshold. Although lasing emission has yet been observed in exciton condensates based on TMD heterostructure system, the realization of exciton BEC suggests the possibility of BEC lasing in the exciton−polariton system after introduction of cavity feedback. Therefore, the development of BEC based on interlayer excitons in TMD heterostructures is feasible to attain electrically pumped lasing based on atomically thin materials with much lower lasing threshold than photonic lasers.

https://dx.doi.org/10.1021/acsmaterialslett.0c00277
ACS Materials Lett. 2020, 2, 1328−1342

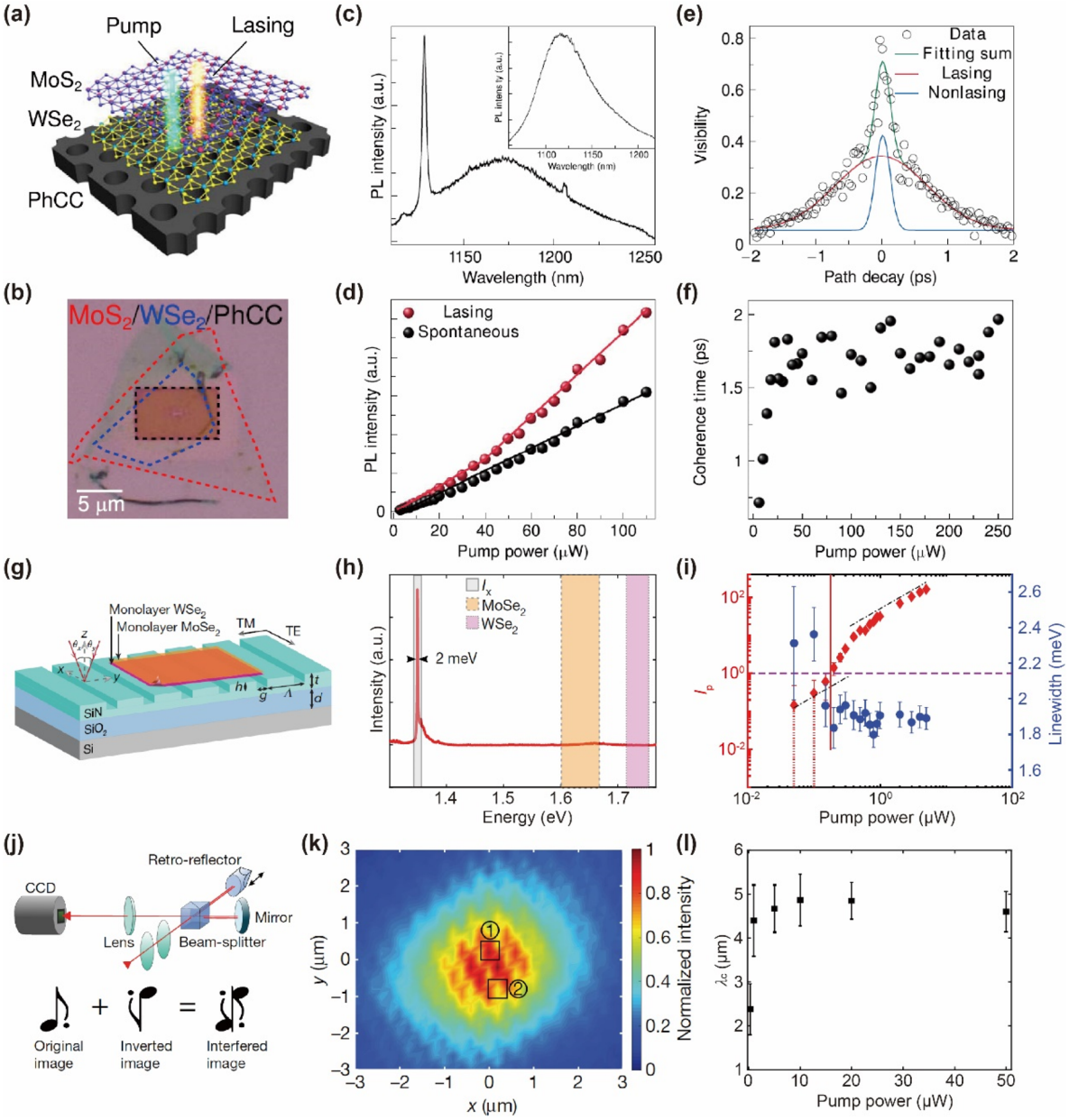

Figure 5. Lasing of interlayer excitons in TMD heterostructures. (a) Scheme of the interlayer-exciton laser constructed by MoS_2/WSe_2 heterostructures onto a photonic crystal cavity. (b) Optical micrograph of MoS_2/WSe_2 heterojunctions onto a photonic crystal. (c) PL spectra of a MoS_2/WSe_2 photonic-crystal laser at room temperature. (d) Output intensity of lasing and spontaneous emission as a function of pump power. (e) Coherent time measurements carried out by a Michelson interferometer present visibility as a function of path decay at pump power of 250 μW. (f) Pump-power-dependent coherence time. Panels a–f: Reproduced from ref 63. Copyright 2019 AAAS. (g) Scheme of a laser based on interlayer excitons constructed by the $WSe_2/MoSe_2$ heterojunction on a grating cavity. (h) PL spectrum of the $WSe_2/MoSe_2$ heterostructure pumped by a 633 nm laser at power of 20 μW. The shading areas highlights the emission from interlayer excitons, $MoSe_2$ and WSe_2, respectively. (i) Output intensity and line width of lasing emissions as a function of pump power. (j) Scheme of a Michelson interferometer for the measurement of first-order coherence of the interlayer-exciton laser. (k) Representative interference pattern at power of 20 μW. (l) Coherence length as a function of pump power. The error bars were introduced by the Gaussian fitting. Panels g–l: Reproduced from ref 65. Copyright 2019 Springer Nature.

As a typical Boson, excitons are possible to condensate at a ground state. Compared to that of the ultracold dilute atom gas, excitons exhibit a much lower effective mass, which permits the realization of BEC at higher temperature. However, the short lifetime of photoexcited excitons has been a major restriction to realize such macroscopic quantum phase in the exciton system. In the past decades, indirect excitons with spatially separated electrons and holes, such as bilayer quantum well systems[114−116] and bilayer graphene isolated by hBN,[117] have been demonstrated with BEC. However, exciton condensation was observed under high magnetic field and ultralow temperature in these systems. Recently, a breakthrough of exciton condensation at relatively high temperature of 190 K has been realized in 1T-$TiSe_2$ semimetals.[118] Kogar et al. demonstrated a transition from an electronic, plasmon-like excitation to an exciton condensate by observing falling of the electronic-mode energy to zero at a non-zero momentum using momentum-resolved electron-energy-loss spectroscopy (M-EELS).[118] These results can

https://dx.doi.org/10.1021/acsmaterialslett.0c00277
ACS Materials Lett. 2020, 2, 1328−1342

unambiguously demonstrate the BEC phase transition and distinguished the exciton condensate phase from the charge density wave phase originating from Peierls distortion. Although the high-temperature exciton condensation has been realized in this work, the semimetal nature of $TiSe_2$ restricts its practical implementations toward electroluminescence devices.

The realization of exciton BEC suggests the possibility of BEC lasing in the exciton−polariton system after introduction of cavity feedback.

2D TMD intralayer/interlayer excitons possess exceptionally high binding energy of several hundreds of millielectronvolts, which supports stable exciton resonance under relatively high concentration ($>10^{12}$ cm^{-2}) at room temperature. In particular, interlayer excitons with much longer lifetimes than those of intralayer excitons are hopeful to achieve BEC at a ground state. In 2019, Shan, Mak, and their colleagues reported BEC of interlayer excitons in $MoSe_2$−WSe_2 atomic double layers separated by few-layer hBN at a relatively high temperature of 100 K.[119] The device was constructed by inserting two- to three-layer hBN tunneling barrier between $MoSe_2$ and WSe_2 (Figure 6a). Gate voltages can be applied to tune the electron/hole concentration in $MoSe_2$/WSe_2 by introducing 20−30 nm hBN as gate dielectrics and few-layer graphene as contact. The reflection spectra of $MoSe_2$−WSe_2 double layers were shown in Figure 6b. At a bias of 5.5 V, a p−n region with excess electrons in $MoSe_2$ and excess holes WSe_2 was observed, which reflected by reflection signals at lower energy. This indicates the electroluminescence of interlayer excitons. Based on this device, a high interlayer exciton concentration up to 10^{12} cm^{-2} can be achieved. The concentration of interlayer excitons is directly related to the tunneling current of the device.

By tuning the gate and bias voltages, the exciton concentration and electroluminescence of $MoSe_2$−WSe_2 double layers can be controlled. Figure 6c illustrates electroluminescence spectra at different exciton concentrations. These spectra show a peak with a FWHM of 10−20 meV originating from the radiative recombination of interlayer excitons. The integrated intensity of electroluminescence spectra and tunneling current as a function of interlayer exciton concentration were plotted in Figure 6e. The electroluminescence intensity presents a clear threshold at ~0.26 × 10^{12} cm^{-2}. Around the threshold, electroluminescence experiences a rapid increase of two orders of magnitude with the two-fold increase of tunneling current. The second-order correlation function $g^{(2)}(\tau)$ was measured using a Hanbury−Brown−Twiss-type setup to study the coherence of electroluminescence as a function of exciton concentration (Figure 6d). Near the threshold, photon bunching with $g^{(2)}(\tau) > 1$ has been observed, which is absent ($g^{(2)}(\tau) = 1$) with the exciton concentration above the threshold. Super-Poissonian photon statistics were observed, indicating the formation of exciton condensation. The threshold behavior together with Poissonian statistics indicates the exciton condensation in $MoSe_2$−WSe_2 double layers.

In this Review, we have summarized the construction of nanolasers based on TMD monolayers and vdW heterostructures incorporated with various optical cavities. Compared to conventional III−V semiconducting quantum wells and dots, TMDs with tightly bound excitons and atomically thin

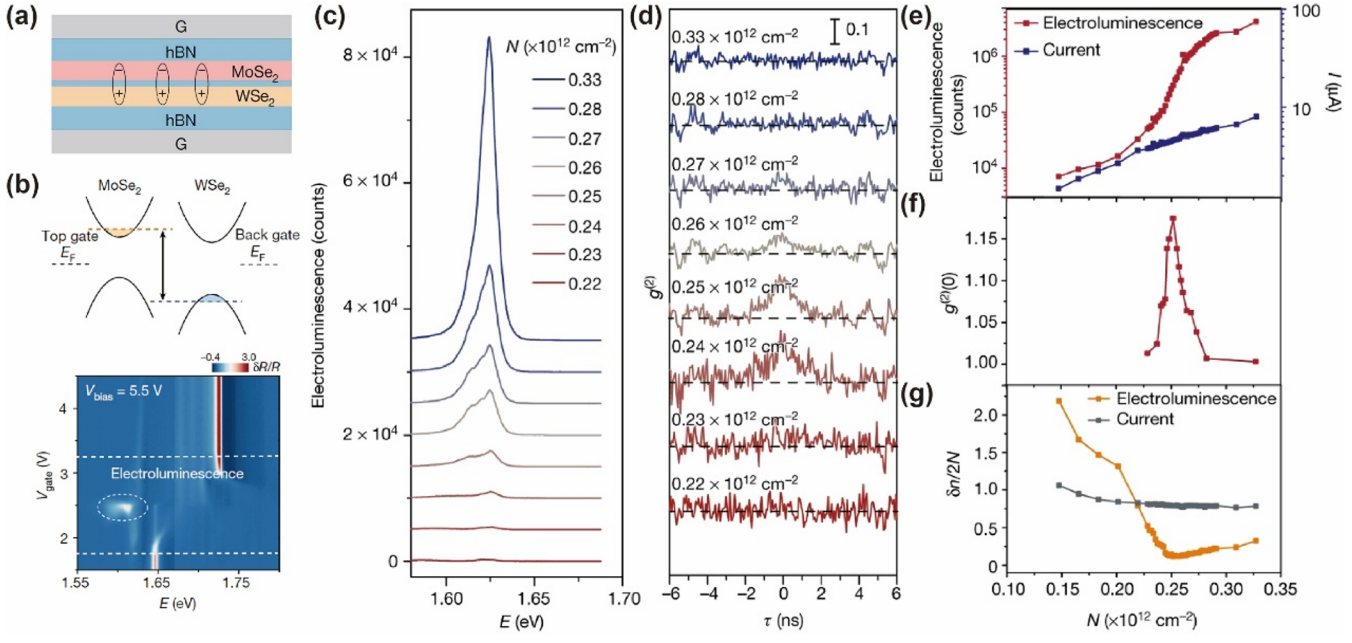

Figure 6. Exciton condensation demonstrated in 2D atomic double layers. (a) Schematic illustration of device configuration. This device is constructed by angle-aligned $MoSe_2$ and WSe_2 separated by two- to three-layer hBN tunneling barrier. The gate electric field is applied at two sides through fabrication of 20−30 nm hBN gate dielectric and few-layer graphene electrode. (b) Reflection contrast $\delta R/R$ at different photon energies as a function of gate voltage under bias voltage of 5.5 V. The upper panel shows band alignment under this condition. (c) Electroluminescence spectra under different exciton concentrations. (d) Second-order correlation function $g^{(2)}(\tau)$ as a function of exciton concentration. The dashed lines highlight the $g^{(2)}(\tau) = 1$. (e) Electroluminescence, (f) $g^{(2)}(\tau)$ at zero time delay, and (g) the electroluminescence and tunneling density width as a function of exciton concentration. Reproduced from ref 119. Copyright 2019 Springer Nature.

https://dx.doi.org/10.1021/acsmaterialslett.0c00277
ACS Materials Lett. 2020, 2, 1328−1342

2D TMD intralayer/interlayer excitons possess an exceptionally high binding energy of several hundreds of millielectronvolts, which supports stable exciton resonance under relatively high concentration at room temperature.

structures are potentially good candidates for the ultracompact nanolasers. Narrowed peaks, clear thresholds and first-order coherence have unambiguously distinguished the lasing emissions from the narrowed emissions caused by other mechanisms.[33,34,63−66] Continuous-wave excitation, room-temperature operation, and relatively low threshold have been realized based on TMD monolayers and vdW heterostructures. Integration of TMD monolayers and heterostructures with silicon photonics has created photonic devices, such as modulators[32] and photodetectors.[120] It is expected that ultracompact integrated photonic circuits can be realized after incorporating nanolasers based on TMD materials.

Despite the rapid progress, it still remains challenging for the practical applications of TMD lasers. At the present, almost all of TMD nanolasers discovered are based on samples exfoliated from bulk crystals. Large-area fabrication of high-quality TMD monolayer and heterostructure thin films onto target substrates is a prerequisite for the on-chip integration of TMD nanolasers. Although the CVD-grown samples on silica fibers have presented the lasing emission,[67] planar integration of coherent light sources requires growth of TMD materials onto planar substrates, such as silicon, Si_3N_4, and silica plates. For TMD monolayers fabricated by mechanical exfoliation from bulk crystals and CVD method, a large defect density gives rise to a relatively low PL quantum yield below 1%.[121,122] These defects have caused serious non-radiative recombination, which usually overwhelms the radiative recombination at the room temperature. In particular, TMD monolayers grown by CVD often possess much higher defect density than their mechanically exfoliated counterparts.[123] Although mechanically exfoliated monolayers often exhibit higher performance, the CVD method plays a pivotal role in the practical device application of TMD monolayers. Therefore, it is significant to develop CVD process to suppress the defect formation and post-treatment techniques for defect passivation. To further decrease the threshold of lasers, rational passivation of traps plays an important role. Some of surface chemical passivation methods have been developed, but high PL quantum yields are only observed under low exciton population and a significant loss of quantum efficiency occurred at high excitation power, which is not suitable for the high-performance lasing applications.

For the practical application of vdW heterostructures, control of crystallographic alignment is an additional requirement. The efficiency of charge transfer and generation of interlayer excitons related to the momentum need to match with each other between the different layers, which has not been extensively investigated in CVD-grown heterostructures. The properties of interlayer excitons in CVD-grown heterostructures have not been well studied and approaches to improve the PL quantum efficiency of interlayer excitons in dash line structures still elusive.

Electrically pumped lasers are another milestone for the development of integrated lasers based on atomically thin TMD heterostructures. At the present stage, continuous-wave lasing emission and electrically injected light-emitting diodes have been realized based on vdW heterostructures. Development of electrically pumped lasing emission requires further optimization of light-emitting layers, charge carrier transport layers and optical cavities. Firstly, improvement of quantum yield by rational passivation is required to realize high quantum efficiency. Secondly, optimization of transport layers and contact between different layers should be carried out to enable the high-intensity charge injection and buildup of enough exciton population to realize lasing emission. Thirdly, conductive optical cavities can be introduced to achieve charge-carrier transport and optical confinement simultaneously. After the realization of electrically pumped lasers, integration of other photonic components, including waveguides, optical modulators and photodetectors, can accelerate the development of ultracompact integrated photonics based on atomically thin TMD materials.

Introduction of spin−valley polarization into lasing emission offers new opportunities to create functional lasing devices. In III−V semiconducting quantum wells, spin polarized lasers have been achieved by employing anisotropic refractive index, magnetic nanoparticles and ferromagnetic Schottky tunnel contact.[101,124,125] Enhanced electron−hole exchange interaction under high population might be the main restriction and the stabilization of spin polarization in TMD materials is still elusive. Fundamental insights into the restriction factors for the valley polarization lifetime are significant for the further development of all valleytronic devices, including the spin-polarized nanolasers.

Development of exciton−polariton lasers based on TMD materials is another important direction to study the low-threshold lasing emission and many-body physics, such as BEC[100] and superfluidity.[126−128] In a semiconducting microcavity, strong coupling of excitons and photons creates a kind of new bosonic quasi-particles termed exciton polariton. With efficient energy relaxation, exciton polaritons is capable to concentrate onto one ground state. The exciton polariton condensates are a typical quasi-equilibrium dissipative system and polaritons present a lifetime of 1−10 ps, which can finally emit coherent photons from the same ground state. Because this process does not require population inversion, polariton lasers often exhibit orders-of-magnitude lower thresholds than photonic lasers. Considerable exciton binding energy of several hundreds of millielectronvolt sustain stable exciton polariton at room temperature, whereas exciton polaritons in GaAs semiconducting quantum wells only stabilize at cryogenic temperature owing to their small exciton binding energy less than 10 meV. Strong coupling and formation of exciton polariton have been demonstrated by incorporating TMD monolayers with DBR microcavities. On the basis of this device configuration, spin−valley accessibility of exciton polariton has been demonstrated and electrical injection of exciton polaritons has been realized by loading vdW heterostructures in optical microcavities. Observation of polariton condensation and superfluidity of TMD monolayers and vdW heterostructures will be an exciting direction to be explored in the future. Combination of unique physical properties of TMD materials with the microcavity exciton polaritons is an intriguing direction to realize the manipulation of polaritons and polaritonic condensates by employing helical light, external electric, and magnetic fields.

https://dx.doi.org/10.1021/acsmaterialslett.0c00277
ACS Materials Lett. 2020, 2, 1328−1342

AUTHOR INFORMATION

Corresponding Author

Ting Yu − *Division of Physics and Applied Physics, School of Physical and Mathematical Sciences, Nanyang Technological University, 637371, Singapore;* orcid.org/0000-0001-5782-1588; Email: yuting@ntu.edu.sg

Authors

Wen Wen − *Division of Physics and Applied Physics, School of Physical and Mathematical Sciences, Nanyang Technological University, 637371, Singapore*

Lishu Wu − *Division of Physics and Applied Physics, School of Physical and Mathematical Sciences, Nanyang Technological University, 637371, Singapore;* orcid.org/0000-0002-2353-9477

Complete contact information is available at: https://pubs.acs.org/10.1021/acsmaterialslett.0c00277

Notes

The authors declare no competing financial interest.

ACKNOWLEDGMENTS

This work is supported by the Ministry of Education of Singapore (MOE 2019-T2-1-044). This work is supported by the Singapore National Research Foundation (NRF) under the Competitive Research Programs (NRF-CRP-21-2018-0007).

REFERENCES

(1) Mak, K. F.; Shan, J. Photonics and Optoelectronics of 2D Semiconductor Transition Metal Dichalcogenides. *Nat. Photonics* **2016**, *10*, 216−226.

(2) Manzeli, S.; Ovchinnikov, D.; Pasquier, D.; Yazyev, O. V.; Kis, A. 2D Transition Metal Dichalcogenides. *Nat. Rev. Mater.* **2017**, *2*, 17033.

(3) Xia, F.; Wang, H.; Xiao, D.; Dubey, M.; Ramasubramaniam, A. Two-Dimensional Material Nanophotonics. *Nat. Photonics* **2014**, *8*, 899−907.

(4) Wang, G.; Chernikov, A.; Glazov, M. M.; Heinz, T. F.; Marie, X.; Amand, T.; Urbaszek, B. Colloquium: Excitons in Atomically Thin Transition Metal Dichalcogenides. *Rev. Mod. Phys.* **2018**, *90*, 021001.

(5) Splendiani, A.; Sun, L.; Zhang, Y.; Li, T.; Kim, J.; Chim, C.-Y.; Galli, G.; Wang, F. Emerging Photoluminescence in Monolayer MoS_2. *Nano Lett.* **2010**, *10*, 1271−1275.

(6) Mak, K. F.; Lee, C.; Hone, J.; Shan, J.; Heinz, T. F. Atomically Thin MoS_2: a New Direct-Gap Semiconductor. *Phys. Rev. Lett.* **2010**, *105*, 136805.

(7) He, K.; Kumar, N.; Zhao, L.; Wang, Z.; Mak, K. F.; Zhao, H.; Shan, J. Tightly Bound Excitons in Monolayer WSe_2. *Phys. Rev. Lett.* **2014**, *113*, 026803.

(8) Chernikov, A.; Berkelbach, T. C.; Hill, H. M.; Rigosi, A.; Li, Y.; Aslan, O. B.; Reichman, D. R.; Hybertsen, M. S.; Heinz, T. F. Exciton Binding Energy and Nonhydrogenic Rydberg Series in Monolayer WS_2. *Phys. Rev. Lett.* **2014**, *113*, 076802.

(9) Schuller, J. A.; Karaveli, S.; Schiros, T.; He, K.; Yang, S.; Kymissis, I.; Shan, J.; Zia, R. Orientation of Luminescent Excitons in Layered Nanomaterials. *Nat. Nanotechnol.* **2013**, *8*, 271−276.

(10) Britnell, L.; Ribeiro, R. M.; Eckmann, A.; Jalil, R.; Belle, B. D.; Mishchenko, A.; Kim, Y.-J.; Gorbachev, R. V.; Georgiou, T.; Morozov, S. V.; Grigorenko, A. N.; Geim, A. K.; Casiraghi, C.; Neto, A. H. C.; Novoselov, K. S. Strong Light-Matter Interactions in Heterostructures of Atomically Thin Films. *Science* **2013**, *340*, 1311−1314.

(11) Xiao, D.; Liu, G.-B.; Feng, W.; Xu, X.; Yao, W. Coupled Spin and Valley Physics in Monolayers of MoS_2 and Other Group-VI Dichalcogenides. *Phys. Rev. Lett.* **2012**, *108*, 196802.

(12) Cao, T.; Wang, G.; Han, W.; Ye, H.; Zhu, C.; Shi, J.; Niu, Q.; Tan, P.; Wang, E.; Liu, B.; Feng, J. Valley-Selective Circular Dichroism of Monolayer Molybdenum Disulphide. *Nat. Commun.* **2012**, *3*, 887.

(13) Mak, K. F.; He, K.; Shan, J.; Heinz, T. F. Control of Valley Polarization in Monolayer MoS_2 by Optical Helicity. *Nat. Nanotechnol.* **2012**, *7*, 494−498.

(14) Zeng, H.; Dai, J.; Yao, W.; Xiao, D.; Cui, X. Valley Polarization in MoS_2 Monolayers by Optical Pumping. *Nat. Nanotechnol.* **2012**, *7*, 490−493.

(15) Kim, J.; Hong, X.; Jin, C.; Shi, S.-F.; Chang, C.-Y. S.; Chiu, M.-H.; Li, L.-J.; Wang, F. Ultrafast Generation of Pseudo-Magnetic Field for Valley Excitons in WSe_2 Monolayers. *Science* **2014**, *346*, 1205−1208.

(16) Jones, A. M.; Yu, H.; Ross, J. S.; Klement, P.; Ghimire, N. J.; Yan, J.; Mandrus, D. G.; Yao, W.; Xu, X. Spin−Layer Locking Effects in Optical Orientation of Exciton Spin in Bilayer WSe_2. *Nat. Phys.* **2014**, *10*, 130−134.

(17) Zhang, J.; Du, L.; Feng, S.; Zhang, R.-W.; Cao, B.; Zou, C.; Chen, Y.; Liao, M.; Zhang, B.; Yang, S. A.; Zhang, G.; Yu, T. Enhancing and Controlling Valley Magnetic Response in MoS_2/WS_2 Heterostructures by All-Optical Route. *Nat. Commun.* **2019**, *10*, 4226.

(18) Schaibley, J. R.; Yu, H.; Clark, G.; Rivera, P.; Ross, J. S.; Seyler, K. L.; Yao, W.; Xu, X. Valleytronics in 2D Materials. *Nat. Rev. Mater.* **2016**, *1*, 16055.

(19) Yang, W.; Shang, J.; Wang, J.; Shen, X.; Cao, B.; Peimyoo, N.; Zou, C.; Chen, Y.; Wang, Y.; Cong, C.; Huang, W.; Yu, T. Electrically Tunable Valley-Light Emitting Diode (vLED) Based on CVD-Grown Monolayer WS_2. *Nano Lett.* **2016**, *16*, 1560−1567.

(20) Feng, S.; Cong, C.; Konabe, S.; Zhang, J.; Shang, J.; Chen, Y.; Zou, C.; Cao, B.; Wu, L.; Peimyoo, N.; Zhang, B.; Yu, T. Engineering Valley Polarization of Monolayer WS_2: A Physical Doping Approach. *Small* **2019**, *15*, 1805503.

(21) Radisavljevic, B.; Radenovic, A.; Brivio, J.; Giacometti, V.; Kis, A. Single-Layer MoS_2 Transistors. *Nat. Nanotechnol.* **2011**, *6*, 147−150.

(22) Cui, X.; Lee, G.-H.; Kim, Y. D.; Arefe, G.; Huang, P. Y.; Lee, C.-H.; Chenet, D. A.; Zhang, X.; Wang, L.; Ye, F.; Pizzocchero, F.; Jessen, B. S.; Watanabe, K.; Taniguchi, T.; Muller, D. A.; Low, T.; Kim, P.; Hone, J. Multi-Terminal Transport Measurements of MoS_2 Using a van der Waals Heterostructure Device Platform. *Nat. Nanotechnol.* **2015**, *10*, 534−540.

(23) Kang, K.; Xie, S.; Huang, L.; Han, Y.; Huang, P. Y.; Mak, K. F.; Kim, C.-J.; Muller, D.; Park, J. High-Mobility Three-Atom-Thick Semiconducting Films with Wafer-Scale Homogeneity. *Nature* **2015**, *520*, 656−660.

(24) Sarkar, D.; Xie, X.; Liu, W.; Cao, W.; Kang, J.; Gong, Y.; Kraemer, S.; Ajayan, P. M.; Banerjee, K. A Subthermionic Tunnel Field-Effect Transistor with an Atomically Thin Channel. *Nature* **2015**, *526*, 91−95.

(25) Fuhrer, M. S.; Hone, J. Measurement of Mobility in Dual-Gated MoS_2 Transistors. *Nat. Nanotechnol.* **2013**, *8*, 146−147.

(26) Li, L.; Yu, Y.; Ye, G. J.; Ge, Q.; Ou, X.; Wu, H.; Feng, D.; Chen, X. H.; Zhang, Y. Black Phosphorus Field-Effect Transistors. *Nat. Nanotechnol.* **2014**, *9*, 372−377.

(27) Ross, J. S.; Klement, P.; Jones, A. M.; Ghimire, N. J.; Yan, J.; Mandrus, D. G.; Taniguchi, T.; Watanabe, K.; Kitamura, K.; Yao, W.; Cobden, D. H.; Xu, X. Electrically Tunable Excitonic Light-Emitting Diodes Based on Monolayer WSe_2 P−N Junctions. *Nat. Nanotechnol.* **2014**, *9*, 268−272.

(28) Baugher, B. W. H.; Churchill, H. O. H.; Yang, Y.; Jarillo-Herrero, P. Optoelectronic Devices based on Electrically Tunable P−N Diodes in a Monolayer Dichalcogenide. *Nat. Nanotechnol.* **2014**, *9*, 262−267.

(29) Ye, Y.; Xiao, J.; Wang, H.; Ye, Z.; Zhu, H.; Zhao, M.; Wang, Y.; Zhao, J.; Yin, X.; Zhang, X. Electrical Generation and Control of the Valley Carriers in a Monolayer Transition Metal Dichalcogenide. *Nat. Nanotechnol.* **2016**, *11*, 598−602.

(30) Withers, F.; Del Pozo-Zamudio, O.; Mishchenko, A.; Rooney, A. P.; Gholinia, A.; Watanabe, K.; Taniguchi, T.; Haigh, S. J.; Geim, A. K.; Tartakovskii, A. I.; Novoselov, K. S. Light-emitting diodes by Band-Structure Engineering in van der Waals Heterostructures. *Nat. Mater.* **2015**, *14*, 301−306.

(31) Sun, Z.; Martinez, A.; Wang, F. Optical Modulators with 2D Layered Materials. *Nat. Photonics* **2016**, *10*, 227−238.

(32) Datta, I.; Chae, S. H.; Bhatt, G. R.; Tadayon, M. A.; Li, B.; Yu, Y.; Park, C.; Park, J.; Cao, L.; Basov, D. N.; Hone, J.; Lipson, M. Low-Loss

Composite Photonic Platform Based on 2D Semiconductor Monolayers. *Nat. Photonics* **2020**, *14*, 256−262.
(33) Wu, S.; Buckley, S.; Schaibley, J. R.; Feng, L.; Yan, J.; Mandrus, D. G.; Hatami, F.; Yao, W.; Vučković, J.; Majumdar, A.; Xu, X. Monolayer Semiconductor Nanocavity Lasers with Ultralow Thresholds. *Nature* **2015**, *520*, 69−72.
(34) Ye, Y.; Wong, Z. J.; Lu, X.; Ni, X.; Zhu, H.; Chen, X.; Wang, Y.; Zhang, X. Monolayer Excitonic Laser. *Nat. Photonics* **2015**, *9*, 733−737.
(35) Geim, A. K.; Grigorieva, I. V. Van der Waals Heterostructures. *Nature* **2013**, *499*, 419−425.
(36) Novoselov, K. S.; Mishchenko, A.; Carvalho, A.; Castro Neto, A. H. 2D Materials and van der Waals Heterostructures. *Science* **2016**, *353*, aac9439.
(37) Hong, X.; Kim, J.; Shi, S.-F.; Zhang, Y.; Jin, C.; Sun, Y.; Tongay, S.; Wu, J.; Zhang, Y.; Wang, F. Ultrafast Charge Transfer in Atomically Thin MoS_2/WS_2 Heterostructures. *Nat. Nanotechnol.* **2014**, *9*, 682−686.
(38) Merkl, P.; Mooshammer, F.; Steinleitner, P.; Girnghuber, A.; Lin, K. Q.; Nagler, P.; Holler, J.; Schüller, C.; Lupton, J. M.; Korn, T.; Ovesen, S.; Brem, S.; Malic, E.; Huber, R. Ultrafast Transition between Exciton Phases in van der Waals Heterostructures. *Nat. Mater.* **2019**, *18*, 691−696.
(39) Chen, H.; Wen, X.; Zhang, J.; Wu, T.; Gong, Y.; Zhang, X.; Yuan, J.; Yi, C.; Lou, J.; Ajayan, P. M.; Zhuang, W.; Zhang, G.; Zheng, J. Ultrafast Formation of Interlayer Hot Excitons in Atomically Thin MoS_2/WS_2 Heterostructures. *Nat. Commun.* **2016**, *7*, 12512.
(40) Liu, Y.; Weiss, N. O.; Duan, X.; Cheng, H.-C.; Huang, Y.; Duan, X. Van der Waals Heterostructures and Devices. *Nat. Rev. Mater.* **2016**, *1*, 16042.
(41) Tartakovskii, A. Excitons in 2D Heterostructures. *Nat. Rev. Phys.* **2020**, *2*, 8−9.
(42) Rivera, P.; Seyler, K. L.; Yu, H.; Schaibley, J. R.; Yan, J.; Mandrus, D. G.; Yao, W.; Xu, X. Valley-Polarized Exciton Dynamics in a 2D Semiconductor Heterostructure. *Science* **2016**, *351*, 688−691.
(43) Rivera, P.; Yu, H.; Seyler, K. L.; Wilson, N. P.; Yao, W.; Xu, X. Interlayer Valley Excitons in Heterobilayers of Transition Metal Dichalcogenides. *Nat. Nanotechnol.* **2018**, *13*, 1004−1015.
(44) Tong, Q.; Yu, H.; Zhu, Q.; Wang, Y.; Xu, X.; Yao, W. Topological Mosaics in Moiré Superlattices of van der Waals Heterobilayers. *Nat. Phys.* **2017**, *13*, 356−362.
(45) Wu, F.; Lovorn, T.; MacDonald, A. H. Topological Exciton Bands in Moiré Heterojunctions. *Phys. Rev. Lett.* **2017**, *118*, 147401.
(46) Yu, H.; Liu, G.-B.; Tang, J.; Xu, X.; Yao, W. Moiré Excitons: From Programmable Quantum Emitter Arrays to Spin-Orbit-Coupled Artificial Lattices. *Sci. Adv.* **2017**, *3*, e1701696.
(47) Calman, E. V.; Fogler, M. M.; Butov, L. V.; Hu, S.; Mishchenko, A.; Geim, A. K. Indirect Excitons in van der Waals Heterostructures at Room Temperature. *Nat. Commun.* **2018**, *9*, 1895.
(48) Stradi, D.; Papior, N. R.; Hansen, O.; Brandbyge, M. Field Effect in Graphene-Based van der Waals Heterostructures: Stacking Sequence Matters. *Nano Lett.* **2017**, *17*, 2660−2666.
(49) Tran, K.; Moody, G.; Wu, F.; Lu, X.; Choi, J.; Kim, K.; Rai, A.; Sanchez, D. A.; Quan, J.; Singh, A.; Embley, J.; Zepeda, A.; Campbell, M.; Autry, T.; Taniguchi, T.; Watanabe, K.; Lu, N.; Banerjee, S. K.; Silverman, K. L.; Kim, S.; Tutuc, E.; Yang, L.; MacDonald, A. H.; Li, X. Evidence for Moiré Excitons in van der Waals Heterostructures. *Nature* **2019**, *567*, 71−75.
(50) Jin, C.; Regan, E. C.; Yan, A.; Iqbal Bakti Utama, M.; Wang, D.; Zhao, S.; Qin, Y.; Yang, S.; Zheng, Z.; Shi, S.; Watanabe, K.; Taniguchi, T.; Tongay, S.; Zettl, A.; Wang, F. Observation of Moiré Excitons in WSe_2/WS_2 Heterostructure Superlattices. *Nature* **2019**, *567*, 76−80.
(51) Alexeev, E. M.; Ruiz-Tijerina, D. A.; Danovich, M.; Hamer, M. J.; Terry, D. J.; Nayak, P. K.; Ahn, S.; Pak, S.; Lee, J.; Sohn, J. I.; Molas, M. R.; Koperski, M.; Watanabe, K.; Taniguchi, T.; Novoselov, K. S.; Gorbachev, R. V.; Shin, H. S.; Fal'ko, V. I.; Tartakovskii, A. I. Resonantly Hybridized Excitons in Moiré Superlattices in van der Waals Heterostructures. *Nature* **2019**, *567*, 81−86.
(52) Ciarrocchi, A.; Unuchek, D.; Avsar, A.; Watanabe, K.; Taniguchi, T.; Kis, A. Polarization Switching and Electrical Control of Interlayer Excitons in Two-Dimensional van der Waals Heterostructures. *Nat. Photonics* **2019**, *13*, 131−136.
(53) Jin, C.; Ma, E. Y.; Karni, O.; Regan, E. C.; Wang, F.; Heinz, T. F. Ultrafast Dynamics in van der Waals Heterostructures. *Nat. Nanotechnol.* **2018**, *13*, 994−1003.
(54) Mak, K. F.; Shan, J. Opportunities and Challenges of Interlayer Exciton Control and Manipulation. *Nat. Nanotechnol.* **2018**, *13*, 974−976.
(55) Ross, J. S.; Rivera, P.; Schaibley, J.; Lee-Wong, E.; Yu, H.; Taniguchi, T.; Watanabe, K.; Yan, J.; Mandrus, D.; Cobden, D.; Yao, W.; Xu, X. Interlayer Exciton Optoelectronics in a 2D Heterostructure p−n Junction. *Nano Lett.* **2017**, *17*, 638−643.
(56) Jauregui, L. A.; Joe, A. Y.; Pistunova, K.; Wild, D. S.; High, A. A.; Zhou, Y.; Scuri, G.; De Greve, K.; Sushko, A.; Yu, C.-H.; Taniguchi, T.; Watanabe, K.; Needleman, D. J.; Lukin, M. D.; Park, H.; Kim, P. Electrical Control of Interlayer Exciton Dynamics in Atomically Thin Heterostructures. *Science* **2019**, *366*, 870−875.
(57) Rivera, P.; Schaibley, J. R.; Jones, A. M.; Ross, J. S.; Wu, S.; Aivazian, G.; Klement, P.; Seyler, K.; Clark, G.; Ghimire, N. J.; Yan, J.; Mandrus, D. G.; Yao, W.; Xu, X. Observation of Long-Lived Interlayer Excitons in Monolayer $MoSe_2−WSe_2$ Heterostructures. *Nat. Commun.* **2015**, *6*, 6242.
(58) Yu, Y.; Hu, S.; Su, L.; Huang, L.; Liu, Y.; Jin, Z.; Purezky, A. A.; Geohegan, D. B.; Kim, K. W.; Zhang, Y.; Cao, L. Equally Efficient Interlayer Exciton Relaxation and Improved Absorption in Epitaxial and Nonepitaxial MoS_2/WS_2 Heterostructures. *Nano Lett.* **2015**, *15*, 486−491.
(59) Yu, H.; Wang, Y.; Tong, Q.; Xu, X.; Yao, W. Anomalous Light Cones and Valley Optical Selection Rules of Interlayer Excitons in Twisted Heterobilayers. *Phys. Rev. Lett.* **2015**, *115*, 187002.
(60) Kim, J.; Jin, C.; Chen, B.; Cai, H.; Zhao, T.; Lee, P.; Kahn, S.; Watanabe, K.; Taniguchi, T.; Tongay, S.; Crommie, M. F.; Wang, F. Observation of Ultralong Valley Lifetime in WSe_2/MoS_2 Heterostructures. *Sci. Adv.* **2017**, *3*, e1700518.
(61) Unuchek, D.; Ciarrocchi, A.; Avsar, A.; Watanabe, K.; Taniguchi, T.; Kis, A. Room-Temperature Electrical Control of Exciton Flux in a van der Waals Heterostructure. *Nature* **2018**, *560*, 340−344.
(62) Wang, Z.; Chiu, Y.-H.; Honz, K.; Mak, K. F.; Shan, J. Electrical Tuning of Interlayer Exciton Gases in WSe_2 Bilayers. *Nano Lett.* **2018**, *18*, 137−143.
(63) Liu, Y.; Fang, H.; Rasmita, A.; Zhou, Y.; Li, J.; Yu, T.; Xiong, Q.; Zheludev, N.; Liu, J.; Gao, W. Room Temperature Nanocavity Laser with Interlayer Excitons in 2D Heterostructures. *Sci. Adv.* **2019**, *5*, eaav4506.
(64) Li, Y.; Zhang, J.; Huang, D.; Sun, H.; Fan, F.; Feng, J.; Wang, Z.; Ning, C. Z. Room-Temperature Continuous-Wave Lasing from Monolayer Molybdenum Ditelluride Integrated with a Silicon Nanobeam Cavity. *Nat. Nanotechnol.* **2017**, *12*, 987−992.
(65) Paik, E. Y.; Zhang, L.; Burg, G. W.; Gogna, R.; Tutuc, E.; Deng, H. Interlayer Exciton Laser of Extended Spatial Coherence in Atomically Thin Heterostructures. *Nature* **2019**, *576*, 80−84.
(66) Shang, J.; Cong, C.; Wang, Z.; Peimyoo, N.; Wu, L.; Zou, C.; Chen, Y.; Chin, X. Y.; Wang, J.; Soci, C.; Huang, W.; Yu, T. Room-Temperature 2D Semiconductor Activated Vertical-Cavity Surface-Emitting Lasers. *Nat. Commun.* **2017**, *8*, 543.
(67) Liao, F.; Yu, J.; Gu, Z.; Yang, Z.; Hasan, T.; Linghu, S.; Peng, J.; Fang, W.; Zhuang, S.; Gu, M.; Gu, F. Enhancing Monolayer Photoluminescence on Optical Micro/Nanofibers for Low-Threshold Lasing. *Sci. Adv.* **2019**, *5*, eaax7398.
(68) Zhang, C.; Gong, C.; Nie, Y.; Min, K.-A.; Liang, C.; Oh, Y. J.; Zhang, H.; Wang, W.; Hong, S.; Colombo, L.; Wallace, R. M.; Cho, K. Systematic Study of Electronic Structure and Band Alignment of Monolayer Transition Metal Dichalcogenides in van der Waals Heterostructures. *2D Mater.* **2017**, *4*, 015026.
(69) Mak, K. F.; McGill, K. L.; Park, J.; McEuen, P. L. The Valley Hall Effect in MoS_2 Transistors. *Science* **2014**, *344*, 1489−1492.
(70) Lee, J.; Mak, K. F.; Shan, J. Electrical Control of the Valley Hall Effect in Bilayer MoS_2 Transistors. *Nat. Nanotechnol.* **2016**, *11*, 421−425.

https://dx.doi.org/10.1021/acsmaterialslett.0c00277
ACS Materials Lett. 2020, 2, 1328−1342

(71) Srivastava, A.; Sidler, M.; Allain, A. V.; Lembke, D. S.; Kis, A.; Imamoğlu, A. Valley Zeeman Effect in Elementary Optical Excitations of Monolayer WSe_2. *Nat. Phys.* **2015**, *11*, 141−147.
(72) Wang, Z.; Mak, K. F.; Shan, J. Strongly Interaction-Enhanced Valley Magnetic Response in Monolayer WSe_2. *Phys. Rev. Lett.* **2018**, *120*, 066402.
(73) Stier, A. V.; McCreary, K. M.; Jonker, B. T.; Kono, J.; Crooker, S. A. Exciton Diamagnetic Shifts and Valley Zeeman Effects in Monolayer WS_2 and MoS_2 to 65 Tesla. *Nat. Commun.* **2016**, *7*, 10643.
(74) Xu, X.; Yao, W.; Xiao, D.; Heinz, T. F. Spin and Pseudospins in Layered Transition Metal Dichalcogenides. *Nat. Phys.* **2014**, *10*, 343−350.
(75) Gong, C.; Zhang, H.; Wang, W.; Colombo, L.; Wallace, R. M.; Cho, K. J. A. P. L. Band Alignment of Two-Dimensional Transition Metal Dichalcogenides: Application in Tunnel Field Effect Transistors. *Appl. Phys. Lett.* **2013**, *103*, 053513.
(76) Hill, M. T.; Gather, M. C. Advances in Small Lasers. *Nat. Photonics* **2014**, *8*, 908.
(77) Samuel, I. D. W.; Namdas, E. B.; Turnbull, G. A. How to Recognize Lasing. *Nat. Photonics* **2009**, *3*, 546−549.
(78) Vahala, K. J. Optical Microcavities. *Nature* **2003**, *424*, 839−846.
(79) Lodahl, P.; Mahmoodian, S.; Stobbe, S. Interfacing Single Photons and Single Quantum Dots with Photonic Nanostructures. *Rev. Mod. Phys.* **2015**, *87*, 347−400.
(80) Ellis, B.; Mayer, M. A.; Shambat, G.; Sarmiento, T.; Harris, J.; Haller, E. E.; Vučković, J. Ultralow-Threshold Electrically Pumped Quantum-Dot Photonic-Crystal Nanocavity Laser. *Nat. Photonics* **2011**, *5*, 297−300.
(81) Strauf, S.; Hennessy, K.; Rakher, M. T.; Choi, Y. S.; Badolato, A.; Andreani, L. C.; Hu, E. L.; Petroff, P. M.; Bouwmeester, D. Self-Tuned Quantum Dot Gain in Photonic Crystal Lasers. *Phys. Rev. Lett.* **2006**, *96*, 127404.
(82) Altug, H.; Englund, D.; Vučković, J. Ultrafast Photonic Crystal Nanocavity Laser. *Nat. Phys.* **2006**, *2*, 484−488.
(83) Tandaechanurat, A.; Ishida, S.; Guimard, D.; Nomura, M.; Iwamoto, S.; Arakawa, Y. Lasing Oscillation in a Three-Dimensional Photonic Crystal Nanocavity with a Complete Bandgap. *Nat. Photonics* **2011**, *5*, 91−94.
(84) Aoki, K.; Guimard, D.; Nishioka, M.; Nomura, M.; Iwamoto, S.; Arakawa, Y. Coupling of Quantum-Dot Light Emission with a Three-Dimensional Photonic-Crystal Nanocavity. *Nat. Photonics* **2008**, *2*, 688−692.
(85) Nomura, M.; Kumagai, N.; Iwamoto, S.; Ota, Y.; Arakawa, Y. Laser Oscillation in a Strongly Coupled Single-Quantum-Dot−Nanocavity System. *Nat. Phys.* **2010**, *6*, 279−283.
(86) Kuramochi, E.; Nozaki, K.; Shinya, A.; Takeda, K.; Sato, T.; Matsuo, S.; Taniyama, H.; Sumikura, H.; Notomi, M. Large-Scale Integration of Wavelength-Addressable All-Optical Memories on a Photonic Crystal Chip. *Nat. Photonics* **2014**, *8*, 474−481.
(87) Molesky, S.; Lin, Z.; Piggott, A. Y.; Jin, W.; Vucković, J.; Rodriguez, A. W. Inverse Design in Nanophotonics. *Nat. Photonics* **2018**, *12*, 659−670.
(88) Tamboli, A. C.; Haberer, E. D.; Sharma, R.; Lee, K. H.; Nakamura, S.; Hu, E. L. Room-Temperature Continuous-Wave Lasing in GaN/InGaN Microdisks. *Nat. Photonics* **2007**, *1*, 61−64.
(89) He, L.; Özdemir, Ş. K.; Zhu, J.; Kim, W.; Yang, L. Detecting Single Viruses and Nanoparticles Using Whispering Gallery Microlasers. *Nat. Nanotechnol.* **2011**, *6*, 428−432.
(90) Zhu, J.; Ozdemir, S. K.; Xiao, Y.-F.; Li, L.; He, L.; Chen, D.-R.; Yang, L. On-Chip Single Nanoparticle Detection and Sizing by Mode Splitting in an Ultrahigh-Q Microresonator. *Nat. Photonics* **2010**, *4*, 46−49.
(91) Rueda, A.; Sedlmeir, F.; Kumari, M.; Leuchs, G.; Schwefel, H. G. L. Resonant Electro-Optic Frequency Comb. *Nature* **2019**, *568*, 378−381.
(92) Zhang, M.; Buscaino, B.; Wang, C.; Shams-Ansari, A.; Reimer, C.; Zhu, R.; Kahn, J. M.; Lončar, M. Broadband Electro-Optic Frequency Comb Generation in a Lithium Niobate Microring Resonator. *Nature* **2019**, *568*, 373−377.
(93) Pöllinger, M.; O'Shea, D.; Warken, F.; Rauschenbeutel, A. Ultrahigh-Q Tunable Whispering-Gallery-Mode Microresonator. *Phys. Rev. Lett.* **2009**, *103*, 053901.
(94) Armani, D. K.; Kippenberg, T. J.; Spillane, S. M.; Vahala, K. J. Ultra-High-Q Toroid Microcavity on a Chip. *Nature* **2003**, *421*, 925−928.
(95) Salehzadeh, O.; Djavid, M.; Tran, N. H.; Shih, I.; Mi, Z. Optically Pumped Two-Dimensional MoS_2 Lasers Operating at Room-Temperature. *Nano Lett.* **2015**, *15*, 5302−5306.
(96) Amani, M.; Lien, D.-H.; Kiriya, D.; Xiao, J.; Azcatl, A.; Noh, J.; Madhvapathy, S. R.; Addou, R.; KC, S.; Dubey, M.; Cho, K.; Wallace, R. M.; Lee, S.-C.; He, J.-H.; Ager, J. W.; Zhang, X.; Yablonovitch, E.; Javey, A. Near-Unity Photoluminescence Quantum Yield in MoS_2. *Science* **2015**, *350*, 1065−1068.
(97) Kim, H.; Lien, D.-H.; Amani, M.; Ager, J. W.; Javey, A. Highly Stable Near-Unity Photoluminescence Yield in Monolayer MoS_2 by Fluoropolymer Encapsulation and Superacid Treatment. *ACS Nano* **2017**, *11*, 5179−5185.
(98) Kim, H.; Ahn, G. H.; Cho, J.; Amani, M.; Mastandrea, J. P.; Groschner, C. K.; Lien, D.-H.; Zhao, Y.; Ager, J. W.; Scott, M. C.; Chrzan, D. C.; Javey, A. Synthetic WSe_2 Monolayers with High Photoluminescence Quantum Yield. *Sci. Adv.* **2019**, *5*, eaau4728.
(99) Lien, D.-H.; Uddin, S. Z.; Yeh, M.; Amani, M.; Kim, H.; Ager, J. W.; Yablonovitch, E.; Javey, A. Electrical Suppression of all Nonradiative Recombination Pathways in Monolayer Semiconductors. *Science* **2019**, *364*, 468−471.
(100) Deng, H.; Haug, H.; Yamamoto, Y. Exciton-Polariton Bose−Einstein Condensation. *Rev. Mod. Phys.* **2010**, *82*, 1489−1537.
(101) Holub, M.; Shin, J.; Saha, D.; Bhattacharya, P. Electrical Spin Injection and Threshold Reduction in a Semiconductor Laser. *Phys. Rev. Lett.* **2007**, *98*, 146603.
(102) Fink, T.; Schade, A.; Höfling, S.; Schneider, C.; Imamoglu, A. Signatures of a Dissipative Phase Transition in Photon Correlation Measurements. *Nat. Phys.* **2018**, *14*, 365−369.
(103) Schneider, C.; Rahimi-Iman, A.; Kim, N. Y.; Fischer, J.; Savenko, I. G.; Amthor, M.; Lermer, M.; Wolf, A.; Worschech, L.; Kulakovskii, V. D.; Shelykh, I. A.; Kamp, M.; Reitzenstein, S.; Forchel, A.; Yamamoto, Y.; Höfling, S. An Electrically Pumped Polariton Laser. *Nature* **2013**, *497*, 348−352.
(104) Slusher, R. E. Laser Technology. *Rev. Mod. Phys.* **1999**, *71*, S471−S479.
(105) Mei, Y.; Weng, G.-E.; Zhang, B.-P.; Liu, J.-P.; Hofmann, W.; Ying, L.-Y.; Zhang, J.-Y.; Li, Z.-C.; Yang, H.; Kuo, H.-C. Quantum Dot Vertical-Cavity Surface-Emitting Lasers Covering the 'Green Gap'. *Light: Sci. Appl.* **2017**, *6*, e16199.
(106) Koschorreck, M.; Gehlhaar, R.; Lyssenko, V. G.; Swoboda, M.; Hoffmann, M.; Leo, K. Dynamics of a High-Q Vertical-Cavity Organic Laser. *Appl. Phys. Lett.* **2005**, *87*, 181108.
(107) Dang, C.; Lee, J.; Breen, C.; Steckel, J. S.; Coe-Sullivan, S.; Nurmikko, A. Red, Green and Blue Lasing Enabled by Single-Exciton Gain in Colloidal Quantum Dot Films. *Nat. Nanotechnol.* **2012**, *7*, 335−339.
(108) Gather, M. C.; Yun, S. H. Bio-optimized Energy Transfer in Densely Packed Fluorescent Protein Enables Near-Maximal Luminescence and Solid-State Lasers. *Nat. Commun.* **2014**, *5*, 5722.
(109) Kasprzak, J.; Richard, M.; Kundermann, S.; Baas, A.; Jeambrun, P.; Keeling, J. M. J.; Marchetti, F. M.; Szymańska, M. H.; André, R.; Staehli, J. L.; Savona, V.; Littlewood, P. B.; Deveaud, B.; Dang, L. S. Bose−Einstein Condensation of Exciton Polaritons. *Nature* **2006**, *443*, 409−414.
(110) Sanvitto, D.; Kéna-Cohen, S. The Road towards Polaritonic Devices. *Nat. Mater.* **2016**, *15*, 1061−1073.
(111) Liu, X.; Galfsky, T.; Sun, Z.; Xia, F.; Lin, E.-c.; Lee, Y.-H.; Kéna-Cohen, S.; Menon, V. M. Strong Light−Matter Coupling in Two-Dimensional Atomic Crystals. *Nat. Photonics* **2015**, *9*, 30−34.
(112) Daskalakis, K. S.; Maier, S. A.; Murray, R.; Kéna-Cohen, S. Nonlinear Interactions in an Organic Polariton Condensate. *Nat. Mater.* **2014**, *13*, 271−278.

https://dx.doi.org/10.1021/acsmaterialslett.0c00277
ACS Materials Lett. 2020, 2, 1328−1342

(113) Su, R.; Diederichs, C.; Wang, J.; Liew, T. C. H.; Zhao, J.; Liu, S.; Xu, W.; Chen, Z.; Xiong, Q. Room-Temperature Polariton Lasing in All-Inorganic Perovskite Nanoplatelets. *Nano Lett.* **2017**, *17*, 3982−3988.
(114) Eisenstein, J.; MacDonald, A. H. Bose−Einstein Condensation of Excitons in Bilayer Electron Systems. *Nature* **2004**, *432*, 691−694.
(115) Nandi, D.; Finck, A.; Eisenstein, J.; Pfeiffer, L.; West, K. Exciton Condensation and Perfect Coulomb Drag. *Nature* **2012**, *488*, 481−484.
(116) Eisenstein, J. Exciton Condensation in Bilayer Quantum Hall Systems. *Annu. Rev. Condens. Matter Phys.* **2014**, *5*, 159−181.
(117) Liu, X.; Watanabe, K.; Taniguchi, T.; Halperin, B. I.; Kim, P. Quantum Hall Drag of Exciton Condensate in Graphene. *Nat. Phys.* **2017**, *13*, 746−750.
(118) Kogar, A.; Rak, M. S.; Vig, S.; Husain, A. A.; Flicker, F.; Joe, Y. I.; Venema, L.; MacDougall, G. J.; Chiang, T. C.; Fradkin, E.; et al. Signatures of Exciton Condensation in a Transition Metal Dichalcogenide. *Science* **2017**, *358*, 1314−1317.
(119) Wang, Z.; Rhodes, D. A.; Watanabe, K.; Taniguchi, T.; Hone, J. C.; Shan, J.; Mak, K. F. Evidence of High-Temperature Exciton Condensation in Two-Dimensional Atomic Double Layers. *Nature* **2019**, *574*, 76−80.
(120) Maiti, R.; Patil, C.; Saadi, M. A. S. R.; Xie, T.; Azadani, J. G.; Uluutku, B.; Amin, R.; Briggs, A. F.; Miscuglio, M.; Van Thourhout, D.; Solares, S. D.; Low, T.; Agarwal, R.; Bank, S. R.; Sorger, V. J. Strain-Engineered High-Responsivity $MoTe_2$ Photodetector for Silicon Photonic Integrated Circuits. *Nat. Photonics* **2020**, *14*, 578.
(121) Wang, H.; Zhang, C.; Rana, F. Ultrafast Dynamics of Defect-Assisted Electron−Hole Recombination in Monolayer MoS_2. *Nano Lett.* **2015**, *15*, 339−345.
(122) Yuan, L.; Huang, L. Exciton Dynamics and Annihilation in WS_2 2D Semiconductors. *Nanoscale* **2015**, *7*, 7402−7408.
(123) Cunningham, P. D.; McCreary, K. M.; Hanbicki, A. T.; Currie, M.; Jonker, B. T.; Hayden, L. M. Charge Trapping and Exciton Dynamics in Large-Area CVD Grown MoS_2. *J. Phys. Chem. C* **2016**, *120*, 5819−5826.
(124) Chen, J.-Y.; Wong, T.-M.; Chang, C.-W.; Dong, C.-Y.; Chen, Y.-F. Self-Polarized Spin-Nanolasers. *Nat. Nanotechnol.* **2014**, *9*, 845−850.
(125) Lindemann, M.; Xu, G.; Pusch, T.; Michalzik, R.; Hofmann, M. R.; Žutić, I.; Gerhardt, N. C. Ultrafast Spin-Lasers. *Nature* **2019**, *568*, 212−215.
(126) Amo, A.; Lefrère, J.; Pigeon, S.; Adrados, C.; Ciuti, C.; Carusotto, I.; Houdré, R.; Giacobino, E.; Bramati, A. Superfluidity of Polaritons in Semiconductor Microcavities. *Nat. Phys.* **2009**, *5*, 805−810.
(127) Sanvitto, D.; Marchetti, F. M.; Szymańska, M. H.; Tosi, G.; Baudisch, M.; Laussy, F. P.; Krizhanovskii, D. N.; Skolnick, M. S.; Marrucci, L.; Lemaître, A.; Bloch, J.; Tejedor, C.; Viña, L. Persistent Currents and Quantized Vortices in a Polariton Superfluid. *Nat. Phys.* **2010**, *6*, 527−533.
(128) Amo, A.; Pigeon, S.; Sanvitto, D.; Sala, V. G.; Hivet, R.; Carusotto, I.; Pisanello, F.; Leménager, G.; Houdré, R.; Giacobino, E.; Ciuti, C.; Bramati, A. Polariton Superfluids Reveal Quantum Hydrodynamic Solitons. *Science* **2011**, *332*, 1167−1170.

https://dx.doi.org/10.1021/acsmaterialslett.0c00277
ACS Materials Lett. 2020, 2, 1328−1342